

Quantum Dots: Theory

Nenad Vukmirović and Lin-Wang Wang
Computational Research Division
Lawrence Berkeley National Laboratory

December 22, 2009

Keywords: Bethe Salpeter equation; configuration interaction; density functional theory; electronic structure; empirical pseudopotentials; $\mathbf{k} \cdot \mathbf{p}$ method; quantum dots; Quantum Monte Carlo; strain; tight-binding.

Synopsis: This review covers the description of the methodologies typically used for the calculation of the electronic structure of self-assembled and colloidal quantum dots. These are illustrated by the results of their application to a selected set of physical effects in quantum dots.

TABLE OF CONTENTS

1. INTRODUCTION

2. SINGLE PARTICLE METHODS

2.1 Density functional theory

2.2 Empirical pseudopotential method

2.3 Tight-binding methods

2.4 $k \cdot p$ method

2.5 The effect of strain

3. MANY-BODY APPROACHES

3.1 Time dependent density functional theory

3.2 Configuration interaction method

3.3 GW and Bethe-Salpeter equation approach

3.4 Quantum Monte Carlo Methods

4. APPLICATION TO DIFFERENT PHYSICAL EFFECTS: some examples

4.1 Electron and hole wave functions

4.2 Intraband optical processes in embedded quantum dots

4.3 Size dependence of the band gap in colloidal quantum dots

4.4 Excitons

4.5 Auger effects

4.6 Electron-phonon interaction

5. CONCLUSIONS

1. INTRODUCTION

In last three decades, remarkable progress in technology has been made, enabling the production of semiconductor structures of nanometer size. This is the length scale where the laws of quantum mechanics rule and a range of new physical effects is manifested. Fundamental laws of physics can be tested on the one hand, while on the other hand many possible applications are rapidly emerging.

The ultimate nanostructure where carriers are confined in all three spatial dimensions is called a quantum dot. In the last 15 years quantum dots have been produced in several different ways in a broad range of semiconductor material systems. The properties of quantum dots and their possible applications are largely dependent on the method they have been obtained with, which can therefore be used as a criterion for classification of different types of quantum dots:

Electrostatic quantum dots. One can fabricate quantum dots by restricting the two dimensional electron gas in a semiconductor heterostructure laterally by electrostatic gates, or vertically by etching techniques [1, 2]. The properties of this type of quantum dots, sometimes termed as electrostatic quantum dots, can be controlled by changing the applied potential at gates, the choice of the geometry of gates or by external magnetic field. The typical size of these dots is of the order of 100 nm.

Self-assembled quantum dots. Self-assembled quantum dots are obtained in heteroepitaxial systems with different lattice constants. During the growth of a layer of one material on top of another, the formation of nanoscale islands takes place [3], if the width of the layer (so called wetting layer) is larger than a certain critical thickness. This growth mode is called Stranski-Krastanov mode. The most common experimental techniques of the epitaxial nanostructure growth are Molecular Beam Epitaxy (MBE) and Metalorganic Chemical Vapor Deposition (MOCVD) [4, 5]. Since the quantum dot material is embedded in another material, we will refer to these dots also as embedded quantum dots. Self-assembled quantum dots typically have lateral dimensions of the order of 15 – 30 nm and height of the order 3 – 7 nm.

Colloidal quantum dots. A very different approach to obtain quantum dots is to synthesize single crystals of the size of a few nanometers, via chemical methods. The dots obtained this way are called nanocrystals or colloidal quantum dots [6]. Their size and shape can be controlled by

the duration, temperature and ligand molecules used in the synthesis [7]. Colloidal quantum dots are typically of spherical shape. They are often smaller than embedded quantum dots with the diameter sometimes as low as $2 - 4$ nm.

Quantum dots have enabled the study of many fundamental physical effects. Electrostatic quantum dots can be controllably charged with a desired number of electrons and therefore the whole periodic system [8] of artificial atoms created, providing a wealth of data from which an additional insight into the many-body physics of fermion systems could be obtained [1]. Single electron transport and Coulomb blockade effects on the one hand, and the regime of Kondo physics on the other hand, have been investigated [9, 10].

One of the most exciting aspects of quantum dot research is certainly the prospect of using the state of the dot (spin state, exciton or charged exciton) as a qubit in quantum information processing. Coherent control of an exciton state in a single dot selected from an ensemble of self-assembled quantum dots has been achieved [11], as well as the manipulation of the spin state in electrostatic quantum dots [12, 13]. The theoretical and experimental progress in the field of spin-related phenomena in quantum dots has been reviewed in [1, 14]. These results appear promising, although the control of a larger number of quantum dot qubits is not feasible yet, mainly due to difficulty of controlling qubit-qubit interactions.

The practical applications of quantum dots certainly do not lag behind these exciting areas of fundamental science with quantum dots. For example, colloidal quantum dots have found several cutting-edge applications such as fluorescent biological labels [15], highly efficient photovoltaic solar cells [16], and nanocrystal based light emitting diodes [6]. Self-assembled quantum dots find the main application as optoelectronic devices - lasers [17], optical amplifiers [18], single photon sources [19, 20] and photodetectors [21, 22, 23].

This review will focus on theoretical methods used for calculation of physical properties of self-assembled and colloidal quantum dots.

2. SINGLE PARTICLE METHODS

While on the one hand, quantum dots seem to be small and simple objects, a look at their structure from the atomistic side reveals their high complexity. Bearing in mind that the lattice constants of the underlying semiconductor materials are typically of the order of 0.5 nm, one can estimate that a single self-assembled quantum dot contains $\sim 10^6$ nuclei and

even a larger number of electrons interacting among each other with long range Coulomb forces. Even the smallest colloidal quantum dots contain thousands of atoms.

This clearly indicates that direct solution of the many body quantum dot Hamiltonian is not a feasible approach and that smart and efficient methods need to be developed. In this Sec. 2, methods that reduce the problem to an effective single-particle equation will be reviewed.

More than two decades ago, Brus introduced [24, 25] a simple effective mass method to calculate ionization energies, electron affinities and optical transition energies in semiconductor nanocrystals. Within Brus's model, the single particle (electron or hole) energies E and wave functions $\psi(\mathbf{r})$ satisfy the Schrödinger's equation given as:

$$\left[-\frac{1}{2m^*}\nabla^2 + P(\mathbf{r}) \right] \psi(\mathbf{r}) = E\psi(\mathbf{r}), \quad (1)$$

where m^* is the electron or hole effective mass. The system of atomic units where the reduced Planck's constant \hbar , the electron mass m_0 and the electron charge e are all equal to 1 was used in Eq. 1 and will be used in what follows. For simplicity, Eq. 1 assumes that the particle must be confined within the dot, i.e. that the potential outside the dot is infinite. This simplifying assumption can be easily relaxed by adding a more realistic confining potential $V_{\text{conf}}(\mathbf{r})$.

$P(\mathbf{r})$ in Eq. 1 is the additional potential caused by the presence of the surface of the quantum dot. It has a certain analogy with electrostatic image potentials in the case when a charge is near the surface of the metal or the interface between two dielectrics. It can be obtained by calculating the interaction energy between a bare electron and its induced screening potential. The extra interaction energy of an electron at \mathbf{r} inside the quantum dot compared to the corresponding value in bulk is then $P(\mathbf{r})$.

To model the two particle excitations (such as for example electron + hole = exciton), Brus introduced an electrostatic interaction energy term among these particles as

$$V(\mathbf{r}_1, \mathbf{r}_2) = \pm \frac{e^2}{\epsilon|\mathbf{r}_1 - \mathbf{r}_2|} \pm P_M(\mathbf{r}_1, \mathbf{r}_2) + P(\mathbf{r}_1) + P(\mathbf{r}_2), \quad (2)$$

where ϵ is the dielectric constant, P_M corresponds to the interaction of the charge of one particle with surface induced polarization potential of the other particle, while the P -terms describe the interaction of the charge of

one particle with its own surface induced polarization potential, as previously described. The plus (minus) sign is for the two particles of the same (opposite) charge. The effective exciton Hamiltonian is then given as

$$H_{\text{exciton}} = -\frac{1}{2m_e}\nabla_e^2 - \frac{1}{2m_h}\nabla_h^2 - \frac{e^2}{\epsilon|\mathbf{r}_e - \mathbf{r}_h|} - P_M(\mathbf{r}_e, \mathbf{r}_h) + P(\mathbf{r}_e) + P(\mathbf{r}_h). \quad (3)$$

The solution of the eigenvalue problem of this Hamiltonian can be written down analytically as:

$$E^* \simeq E_g + \frac{\pi^2}{2R^2}\left[\frac{1}{m_e} + \frac{1}{m_h}\right] - \frac{\alpha_c e^2}{\epsilon R} + \text{small term}, \quad (4)$$

where $\alpha_c = 2 - \frac{\text{Si}(2\pi)}{\pi} + \frac{\text{Si}(4\pi)}{2\pi} \approx 1.8$ and $\text{Si}(x)$ is the sine integral function $\text{Si}(x) = \int_0^x \frac{\sin t}{t} dt$. The last term in Eq. 4 originates from the last three terms in Eq. 3. One should note that $P(\mathbf{r}) = P_M(\mathbf{r}, \mathbf{r})/2$, therefore $P_M(\mathbf{r}_e, \mathbf{r}_h)$ and $P(\mathbf{r}_e) + P(\mathbf{r}_h)$ cancel out exactly when $\mathbf{r}_e = \mathbf{r}_h$ and lead to a small term when \mathbf{r}_e and \mathbf{r}_h are not equal. This small term can often be ignored in practice for spherical quantum dots.

The cancellation of the polarization terms gives as a guide for a general approach for calculating the excitons in nanocrystals. As a first step, one calculates the single particle energies from Eq. 1 without the polarization term. As a second step, the screened electron-hole interaction is added perturbatively. One should however have in mind that such an approach is an approximation based on classical electrostatic consideration. It ignores the effects such as dynamic screening and the local field effects of the dielectric function. The single particle states obtained this way are not the quasi-particles from the usual GW formalism (The eigenenergies of Eq. 1 with the P -term are the quasi particle energies that correspond to the electron affinity and ionization potential.). However, such single particle states are the natural extension of single-particle states considered in other nanostructures, such as quantum wells and superlattices. These are also fully in line with eigen states defined in the density functional theory discussed below. The rest of Sec. 2 will therefore be completely devoted to the theoretical frameworks and methodologies for calculating these states.

2.1 Density functional theory

Within the density functional theory (DFT) [26], the many-body Hamiltonian problem reduces to a set of single particle Kohn-Sham equations [27]

that read

$$\left(-\frac{1}{2}\nabla^2 + V_{\text{ion}} + V_{\text{H}} + V_{\text{XC}}\right)\psi_i(\mathbf{r}) = \epsilon_i\psi_i(\mathbf{r}). \quad (5)$$

In the above equation $\psi_i(\mathbf{r})$ and ϵ_i are the wave functions and energies of Kohn-Sham orbitals, $V_{\text{ion}}(\mathbf{r})$ is the potential of all nuclei in the system, $V_{\text{H}}(\mathbf{r})$ is the Hartree potential of electrons given as

$$V_{\text{H}}(\mathbf{r}) = \int d\mathbf{r}' \frac{\rho(\mathbf{r}')}{|\mathbf{r} - \mathbf{r}'|}, \quad (6)$$

where

$$\rho(\mathbf{r}) = \sum |\psi_i(\mathbf{r})|^2 \quad (7)$$

is the electronic charge density of the system. The summation in Eq. (7) goes over all occupied Kohn-Sham orbitals. The exchange-correlation potential V_{XC} in Eq. (5) is supposed to take into account all the other effects of electron-electron interactions beyond the simple Coulomb repulsion (described in V_{H}). The exact form of this potential is not known and it needs to be approximated. The most widely used approximation is the local density approximation (LDA) where it is assumed that V_{XC} depends only on the local electronic charge density and takes the same value as in the free electron gas of that density [27]. Eqs. 5 and 7 need to be solved self-consistently until the convergence is achieved.

Density functional theory calculations are still computationally demanding, partly due to the necessity of self consistent calculations. One also needs to calculate all the orbitals ψ_i in each iteration, while in semiconducting systems one is often interested in only a few states in the region around the gap that determine the optical and transport properties of the system.

An alternative approach that avoids the full self-consistent calculation without loss in accuracy is the charge patching method (CPM) [28, 29, 30, 31, 32, 33]. The basic assumption of the CPM is that the charge density around a given atom depends only on the local atomic environment around the atom. This is true if there is no long range external electric field that causes long-range charge transfer. This is often satisfied if there is a band gap in the material. Based on this assumption, the idea is to calculate (using DFT in LDA for example) the charge density of some small prototype system $\rho_{\text{LDA}}(\mathbf{r})$, decompose it into contributions from individual atoms (charge density motifs) and then use these motifs to patch the charge density of a large system.

In particular, charge density motifs are calculated from the charge density of the prototype system as:

$$m_{I_\alpha}(\mathbf{r} - \mathbf{R}_\alpha) = \rho_{LDA}(\mathbf{r}) \frac{w_\alpha(|\mathbf{r} - \mathbf{R}_\alpha|)}{\sum_{\mathbf{R}_{\alpha'}} w_{\alpha'}(|\mathbf{r} - \mathbf{R}_{\alpha'}|)} \quad (8)$$

where \mathbf{R}_α is the position of atom type α , and $m_{I_\alpha}(\mathbf{r} - \mathbf{R}_\alpha)$ is the charge density motif of this atom type. $w_\alpha(r)$ is an exponentially decaying function, that defines the partition function $w_\alpha(|\mathbf{r} - \mathbf{R}_\alpha|)/\sum_{\mathbf{R}_{\alpha'}} w_{\alpha'}(|\mathbf{r} - \mathbf{R}_{\alpha'}|)$ that divides the space into (mutually overlapping) regions assigned to each atom. $m_{I_\alpha}(\mathbf{r} - \mathbf{R}_\alpha)$ is therefore a localized function that can be stored in a fixed size numerical array. I_α denotes the atomic bonding environment of the atom α . After the charge density motifs are obtained from small prototype systems, the total charge density of the large nanosystem is obtained simply as the sum of motifs assigned to each of the atoms:

$$\rho_{\text{patch}}(\mathbf{r}) = \sum_{\mathbf{R}_\alpha} m_{I_\alpha}(\mathbf{r} - \mathbf{R}_\alpha). \quad (9)$$

Once the charge density is obtained using the charge patching procedure, the single particle Hamiltonian can be generated by solving the Poisson equation for the Hartree potential and using the LDA formula for the exchange-correlation potential. The energies and wave functions of a few states around the gap can then be found using the methods developed to find a few eigenvalues of the Hamiltonian only, such as the folded spectrum method [34] (that will be described in Sec. 2.2).

The charge patching method was used to generate the charge densities of carbon fullerenes [33], semiconductor alloys [28], semiconductor impurities [29], organic molecules and polymers [35], and semiconductor quantum dots [32]. The resulting patched charge density is typically within 1% of the self-consistently calculated LDA charge density, and the corresponding energies are within 30 meV. Typical numerical uncertainty (due to basis function truncations and different nonlocal pseudopotential treatments) of an LDA calculation is about the same order of magnitude. Therefore, the charge patching method can be considered to be as accurate as the direct *ab initio* calculations.

There are however cases where charge patching method cannot be used. One example is the total dipole moment of an asymmetric quantum dot [36]. Such a dipole moment can also induce an internal electric field, and cause the long range charge transfer in the system. It is therefore necessary

to solve the charge density selfconsistently, which can be done using the DFT/LDA method. However, a much more efficient linear scaling method to do such calculations has been developed recently: the linear scaling three dimensional fragment (LS3DF) method [37]. Within the LS3DF method, the system is divided into many small fragments. The wave functions and charge densities of each fragment are calculated separately, each within the standard DFT/LDA method, using a group of a small number of computer processors. After the fragment charge densities are obtained, they are patched together to get the charge density of the whole system using a novel scheme that ensures that the artificial surface effects due to the system subdivision will be cancelled out among the fragments. The patched charge density is then used to solve a global Poisson equation for the global potential. An outside loop is iterated which yields the selfconsistency between the global charge density and the input potential. Due to the use of this novel patching scheme, the LS3DF is very accurate, with its results (including the dipole moments) essentially the same as the original direct DFT calculation results [37], but with potentially thousand times speed ups, for systems with more than ten thousand atoms. As the system grows larger, there are more fragments (while the fragment size is fixed), thus more processor groups can be used to solve them. This provides a perfect parallelization to the number of processors. Meanwhile the total computational cost is proportional to the number of fragments, and consequently the total number of atoms.

A well known problem of the LDA based calculations is that the band gap is severely underestimated [38, 39]. DFT is rigorously only valid for ground state properties, and there is no physical meaning for the Kohn-Sham eigen energies [27]. This conceptual difficulty can be circumvented by using time-dependent DFT which will be discussed later. In practice however, one often restricts to the simple empirical ways to correct the band gap error. One such way is to slightly modify the LDA Hamiltonian to fit the crystal bulk band structure, which can be done for example by changing the s , p , d nonlocal pseudopotentials [29] to move the position of the conduction band while keeping the position of the valence band unchanged. This approach is based on the assumption that the valence band alignment predicted by the LDA is reliable.

For the treatment of colloidal quantum dots, one also has to take care of the quantum dot surface. The surface of an unpassivated nanocrystal consists of dangling bonds that introduce band gap states. One way to remove these states is to pair the dangling bond electron with other electrons. If a surface atom has m valence electrons, this atom provides $m/4$ electrons to

each of its four bonds in a tetrahedral crystal. To pair $m/4$ electrons in a dangling bond, a passivating agent should provide $2 - m/4$ additional electrons. To keep the system locally neutral, there must be a positive $2 - m/4$ nuclear charge nearby. The simplest passivation agent can therefore be a hydrogenlike atom with $2 - m/4$ electrons and a nuclear charge $Z = 2 - m/4$. For IV-IV group materials like Si, this is a $Z = 1$ hydrogen atom. For III-V and II-VI systems, the resulting atoms have a noninteger Z , consequently these are pseudohydrogen atoms. These artificial pseudohydrogen atoms do describe the essential features of good passivation agents and serve as simplified models for the real passivation situations, where organic molecules with complicated and often unknown structure are involved.

2.2 Empirical pseudopotential method

The empirical pseudopotential method (EPM) was introduced in 1960s by Cohen *et.al.* [40, 41] to fit the band structure of bulk semiconductors. Within the EPM, the Schrödinger equation is given as:

$$[-\frac{1}{2}\nabla^2 + V(\mathbf{r})]\psi_i(\mathbf{r}) = E_i\psi_i(\mathbf{r}) \quad (10)$$

with

$$V(\mathbf{r}) = \sum_{atom} v_{atom}(|\mathbf{r} - \mathbf{R}_{atom}|), \quad (11)$$

where \mathbf{R}_{atom} are the positions of the atoms and $v_{atom}(r)$ are spherical atomic potentials that in an effective manner take into account the effects of nuclei, core and valence electrons. The great success of the EPM was that it was actually possible to fit the band structure of the semiconductors using this single particle approach.

In the EPM calculations, the plane wave representation is typically used, i.e. the wave function is expanded as a linear combination of plane waves, where the summation is restricted only to reciprocal lattice \mathbf{q} vectors with kinetic energy smaller than certain predefined value E_{cut} . To evaluate the resulting Hamiltonian matrix in plane wave representation, Fourier transforms of atomic potentials $v_{atom}(|\mathbf{q}|)$ are needed. Only a few of these are non zero. These are used as adjustable parameters to fit the semiconductor band structure.

To apply the EPM to nanostructures, one needs to have a continuous $v_{atom}(q)$ curve, since the supercell is very large then and consequently \mathbf{q}

points are very dense. The continuous $v_{atom}(q)$ can be represented by a function of 4 parameters $a_1 - a_4$

$$v(q) = \frac{a_1 (q^2 - a_2)}{a_3 e^{a_4 q^2} - 1}$$

or a sum of Gaussians

$$v(q) = \sum a_i e^{-c_i (q - b_i)^2}.$$

For a full description of the colloidal quantum dots, the pseudopotentials of surface passivating hydrogen or pseudohydrogen atoms need to be fitted as well. The pseudopotentials are fitted to experimental data and first principles calculations of bulk band structures, clean surface work function, and the density of states of chemisorbed surfaces.

Another approach to fit the pseudopotentials is to fit them directly to the LDA calculated potential [42] and then modify them slightly to correct the band gap error. The $v_{atom}(q)$ obtained in such a manner are able to fit the bandstructure within 0.1 eV and have in the same time a 99% overlap with the original LDA wavefunction. This approach, called the semi-empirical pseudopotential method (SEPM) has been applied to CdSe [42], InP [43] and Si [42] nanostructures, representing II-VI, III-V, and IV-IV semiconductor systems respectively.

With the empirical or semi-empirical pseudopotentials at hand, one is able to construct the single particle Hamiltonian. The diagonalization of this Hamiltonian is a routine task in the case of bulk semiconductors due to a small number of atoms in a supercell. However, this is no longer the case in quantum dots which contain a large number of atoms. Even the conventional conjugate gradient method [44] which is often used in *ab initio* calculations cannot be used since it scales as $O(N^3)$ due to an orthogonalization step which is a necessary part of the algorithm. Fortunately, for the analysis of most electronic, transport and optical properties of semiconductor nanosystems, only the states in the spectral region close to the band gap are relevant and there is no need to find all the eigenstates of the Hamiltonian. The "folded spectrum method" (FSM), specialized to find the eigenstates in a certain spectral region only, has therefore been developed by Wang and Zunger [34]. The method is based on the fact that the Hamiltonians H and $(H - E_{\text{ref}})^2$ have the same eigenvectors and that the few lowest eigenvectors of $(H - E_{\text{ref}})^2$ are the eigenvectors of H closest to the energy E_{ref} . The lowest eigenstates of $(H - E_{\text{ref}})^2$ are then solved using

the conjugate gradient method. It turns out that the use of $(H - E_{\text{ref}})^2$ compared to H slows down the convergence but with the use of preconditioners and a large number of iterations, convergence can still be achieved. The folded spectrum method within the plane wave representation has been implemented in the parallel code PESCAN [45]. It can be routinely used to calculate systems with a few thousand atoms, or even near million atom systems [46]. Since only a few wavefunctions are calculated, the computational effort scales linearly to the size of the system. Linear scaling method for the calculation of the total and local electronic density of states and the optical absorption spectrum has been developed by Wang [47]. We refer the reader to Ref. [47] for the description of this method, called the generalized moments method (GMM).

Another method for solution of the EPM Hamiltonian is the linear combination of bulk Bloch bands (LCBB) method [48]. The disadvantage of the plane-wave expansion is that it does not lend itself to systematic approximations. A basis set in which such approximations can be naturally made is the basis of full zone bulk Bloch states. In this basis the wavefunction expansion reads

$$\psi(\mathbf{r}) = \sum_n^{N_B} \sum_{\mathbf{k}}^{N_{\mathbf{k}}} C_{\mathbf{k},n} \phi_{\mathbf{k}n}^0(\mathbf{r}), \quad (12)$$

where

$$\phi_{\mathbf{k}n}^0(\mathbf{r}) = \frac{1}{\sqrt{N}} u_{\mathbf{k}n}(\mathbf{r}) e^{i\mathbf{k}\cdot\mathbf{r}} \quad (13)$$

is the bulk Bloch function of the constituent bulk solid, where n is the band index, \mathbf{k} is the supercell reciprocal-lattice vector, N the number of primary cells in the supercell. The LCBB expansion allows one to select the physically important bands n and \mathbf{k} -points. As a result, the number of basis functions can be reduced significantly compared to the plane-wave basis. It turns out that it is possible to use a fixed number of basis functions to achieve the same degree of accuracy for different system sizes, in contrast to the plane-wave basis where the number of basis functions scales linearly with system size. The origin of this effect is the fact that when the size of the system increases the envelope function of the electronic state becomes smoother and therefore the maximum value of the \mathbf{k} -vector needed to represent it becomes smaller. This makes the LCBB method ideal for studying very large systems such as embedded quantum dots.

2.3 Tight-binding methods

The tight-binding (TB) method [49] is the simplest method which still includes the atomic structure of a quantum dot in the calculation [50, 51, 52, 53]. In the TB method one selects the most relevant atomic-like orbitals $|i\alpha\rangle$ localized on atom i , that are assumed to be orthonormal. The single particle wave function is expanded in the basis of these localized orbitals as

$$|\psi\rangle = \sum_{i\alpha} c_{i\alpha} |i\alpha\rangle \quad (14)$$

and therefore the TB single-particle Hamiltonian is of the form

$$H = \sum_{i\alpha} \varepsilon_{i\alpha} |i\alpha\rangle\langle i\alpha| + \frac{1}{2} \sum_{i\alpha, j\beta} t_{i\alpha, j\beta} |i\alpha\rangle\langle j\beta|, \quad (15)$$

where $\varepsilon_{i\alpha}$ are the energies of the orbitals (the on-site energies), while $t_{i\alpha, j\beta}$ are the hopping integrals between different orbitals, that can be restricted to include only nearest neighbors or next nearest neighbors. For the sake of notational simplicity, the form which does not include the spin-orbit interaction and therefore does not mix the states of different spin was presented. The extension to include spin-orbit interaction is straightforward. The most popular flavor of TB is the empirical TB where the parameters of the Hamiltonian are treated as phenomenological and fitted to reproduce the bulk band structure obtained from experiment or higher level calculations. In such an approach the atomic orbitals are not treated explicitly, since the whole spectrum of the single particle Hamiltonian is determined by the on-site energies and hopping integrals. The wavefunction is represented by the coefficients $c_{i\alpha}$ which slowly vary from site to site.

In the TB method, one restricts the atomic orbitals included to only a few for each atom. Since one is typically interested in states around the energy gap, one has to select the orbitals that define these states. In III-V, IV-IV and II-VI semiconductors, these are typically the s , p_x , p_y , p_z orbitals and sometimes d orbitals. Quite often, an additional s -like orbital called s^* is added to provide an additional degree of freedom in fitting of the TB parameters, which leads to models such as sp^3s^* [54] and $sp^3d^5s^*$ [55]. In these models, the size of the resulting Hamiltonian matrix is $nN \times nN$, where N is the number of atoms and n is the number of orbitals per atom ($n = 10$ for sp^3s^* with spin and $n = 20$ for $sp^3d^5s^*$ with spin). Due to nearest neighbors approximation, the matrix is sparse and efficient methods for the diagonalization of sparse matrices can therefore be exploited.

One problem of the TB method is the lack of explicit basis functions. Although these can be added after the TB eigenstates have been calculated,

these basis functions are not an intrinsic part of the TB Hamiltonian and its fitting process, thus their compatibility is an issue. This causes problems to calculate physical properties like dipole transitions and Coulomb and exchange interactions. Another issue in treating quantum dot heterostructures is how to choose the parameters at the interface of two materials, since only the parameters for bulk materials are available. An approximation needs to be introduced, usually by assuming the parameters at the interface as a certain average of the TB parameters of the two materials. In colloidal quantum dots, the surface has to be passivated. Here, we give an example how this is done in the case of *Si* nanocrystals. The surface is passivated by *H* atoms, where the TB nearest-neighbor matrix elements V_{H-Si} between *H* and *Si* are scaled from the *Si-Si* matrix elements V_{Si-Si} according to the Harrison's rule [56]: $V_{H-Si} = V_{Si-Si}(d_{Si-Si}/d_{H-Si})^2$, where d_{Si-Si} and d_{H-Si} are the bond distances [57]. Another way to treat the surface passivation is simply to remove the dangling bond states from the calculated results or even from the Hamiltonian before the matrix is diagonalized. This is done by removing the hybrid sp^3 dangling bond orbital from the TB Hamiltonian basis set (e.g. by removing the Hamiltonian matrix columns and rows expanded by these sp^3 basis) [58]. This is a unique way of artificial passivation only applicable to TB calculations. The ability to describe the surface atomistically is a big advantage of the TB model compared to the $\mathbf{k} \cdot \mathbf{p}$ model, that will be described next.

2.4 $\mathbf{k} \cdot \mathbf{p}$ method

The previously described methods treat explicitly the atomistic details of the nanostructure which therefore leads to their high accuracy and reliability but also to a significant computational cost. In the $\mathbf{k} \cdot \mathbf{p}$ method, central quantities are the slowly varying envelope functions that modulate the rapidly varying atomistic wave function. Historically, $\mathbf{k} \cdot \mathbf{p}$ method was introduced to describe the bulk band structure around a certain special point in the Brillouin zone and later on it was extended to describe the heterostructures.

Let the Hamiltonian of an electron in a semiconductor be

$$\hat{H} = \frac{\hat{\mathbf{p}}^2}{2} + V_0(\mathbf{r}) + \hat{H}_{\text{so}}, \quad (16)$$

where $\hat{\mathbf{p}}$ is the momentum operator, $V_0(\mathbf{r})$ the crystal potential (including nuclei, core electrons and self-consistent potential of valence electrons), and

\hat{H}_{so} the spin-orbit interaction Hamiltonian arising from relativistic corrections to Schrödinger equation given by

$$\hat{H}_{\text{so}} = \frac{\alpha^2}{4} [\nabla V_0(\mathbf{r}) \times \hat{\mathbf{p}}] \cdot \boldsymbol{\sigma}, \quad (17)$$

where α is the fine structure constant and $\boldsymbol{\sigma}$ is a vector of Pauli matrices

$$\sigma_x = \begin{bmatrix} 0 & 1 \\ 1 & 0 \end{bmatrix}, \sigma_y = \begin{bmatrix} 0 & -i \\ i & 0 \end{bmatrix}, \sigma_z = \begin{bmatrix} 1 & 0 \\ 0 & -1 \end{bmatrix}. \quad (18)$$

The envelope representation of the wavefunction of an electron is given by

$$\Psi(\mathbf{r}) = \sum_i \psi_i(\mathbf{r}) u_i(\mathbf{r}), \quad (19)$$

where $u_i(\mathbf{r})$ form the complete orthonormal set of functions with periodicity of the Bravais lattice and $\psi_i(\mathbf{r})$ are slowly varying envelope functions. The most common choice of the functions u_i are bulk Bloch functions at the Γ point. After the replacement of (19) in the Schrödinger equation and making an approximation that eliminates the non-local terms that appear in the derivation, one arrives at [59, 60]

$$-\frac{1}{2} \nabla^2 \psi_m(\mathbf{r}) + \sum_n (-i) \mathbf{p}_{mn} \cdot \nabla \psi_n(\mathbf{r}) + \sum_n H_{mn}(\mathbf{r}) \psi_n(\mathbf{r}) = E \psi_m(\mathbf{r}). \quad (20)$$

Since the second term in Eq. (20) is crucial in determining the Hamiltonian matrix (and $(-i)\nabla$ becomes the \mathbf{k} vector if for example the envelope function is expanded in plane waves), the method being described is called the $\mathbf{k} \cdot \mathbf{p}$ method. The terms in the previous equation are given by

$$\mathbf{p}_{mn} = \frac{1}{\Omega} \int u_m(\mathbf{r})^* \hat{\mathbf{p}} u_n(\mathbf{r}) d^3\mathbf{r}, \quad (21)$$

where the integration goes over the volume of the crystal unit cell Ω , and $H_{mn}(\mathbf{r})$ is the term that, away from the interfaces, reduces to the bulk matrix elements of the Hamiltonian

$$H_{mn} = \frac{1}{\Omega} \int u_m(\mathbf{r})^* \hat{H} u_n(\mathbf{r}) d^3\mathbf{r} = E_m \delta_{mn}, \quad (22)$$

where E_m is the band edge of band m . In practice, one has to restrict to a finite number of bands. Historically, the $\mathbf{k} \cdot \mathbf{p}$ method was first applied

to valence band (6-band Hamiltonian) [61, 62] and later on the conduction band was added (8-band Hamiltonian) [63].

The explicit form of the 8-band Hamiltonian for the crystals with zincblende structure (such as for example InAs, GaAs, AlSb, CdTe, GaP, GaSb, InP, InSb, ZnS, ZnSe, and ZnTe) is given below. This Hamiltonian also perturbatively includes the effect of remote bands. Since the point T_d symmetry group of the zincblende crystal is a subgroup of the diamond group of Ge and Si, the same $\mathbf{k} \cdot \mathbf{p}$ Hamiltonian can be applied to these semiconductors, as well. In the basis $|JJ_z\rangle$ that diagonalises the bulk Hamiltonian at $\mathbf{k} = 0$:

$$\begin{aligned}
|1\rangle &= \left|\frac{1}{2}, -\frac{1}{2}\right\rangle = |S \downarrow\rangle, \\
|2\rangle &= \left|\frac{1}{2}, \frac{1}{2}\right\rangle = |S \uparrow\rangle, \\
|3\rangle &= \left|\frac{3}{2}, \frac{1}{2}\right\rangle = -\frac{i}{\sqrt{6}}|(X + iY) \downarrow\rangle + i\sqrt{\frac{2}{3}}|Z \uparrow\rangle, \\
|4\rangle &= \left|\frac{3}{2}, \frac{3}{2}\right\rangle = \frac{i}{\sqrt{2}}|(X + iY) \uparrow\rangle, \\
|5\rangle &= \left|\frac{3}{2}, -\frac{3}{2}\right\rangle = -\frac{i}{\sqrt{2}}|(X - iY) \downarrow\rangle, \\
|6\rangle &= \left|\frac{3}{2}, -\frac{1}{2}\right\rangle = \frac{i}{\sqrt{6}}|(X - iY) \uparrow\rangle + i\sqrt{\frac{2}{3}}|Z \downarrow\rangle, \\
|7\rangle &= \left|\frac{1}{2}, -\frac{1}{2}\right\rangle = -\frac{i}{\sqrt{3}}|(X - iY) \uparrow\rangle + \frac{i}{\sqrt{3}}|Z \downarrow\rangle, \\
|8\rangle &= \left|\frac{1}{2}, \frac{1}{2}\right\rangle = -\frac{i}{\sqrt{3}}|(X + iY) \downarrow\rangle - \frac{i}{\sqrt{3}}|Z \uparrow\rangle,
\end{aligned} \tag{23}$$

the 8-band $\mathbf{k} \cdot \mathbf{p}$ Hamiltonian reads (where the definition $\mathbf{k} = -i\nabla$ was introduced)

$$\hat{H}_k = \tag{24}$$

$$\begin{bmatrix} A & 0 & V^+ & 0 & \sqrt{3}V & -\sqrt{2}U & -U & \sqrt{2}V^+ \\ 0 & A & -\sqrt{2}U & -\sqrt{3}V^+ & 0 & -V & \sqrt{2}V & U \\ V & -\sqrt{2}U & -P+Q & -S^+ & R & 0 & \sqrt{\frac{3}{2}}S & -\sqrt{2}Q \\ 0 & -\sqrt{3}V & -S & -P-Q & 0 & R & -\sqrt{2}R & \frac{1}{\sqrt{2}}S \\ \sqrt{3}V^+ & 0 & R^+ & 0 & -P-Q & S^+ & \frac{1}{\sqrt{2}}S^+ & \sqrt{2}R^+ \\ -\sqrt{2}U & -V^+ & 0 & R^+ & S & -P+Q & \sqrt{2}Q & \sqrt{\frac{3}{2}}S^+ \\ -U & \sqrt{2}V^+ & \sqrt{\frac{3}{2}}S^+ & -\sqrt{2}R^+ & \frac{1}{\sqrt{2}}S & \sqrt{2}Q & -P-\Delta & 0 \\ \sqrt{2}V & U & -\sqrt{2}Q & \frac{1}{\sqrt{2}}S^+ & \sqrt{2}R & \sqrt{\frac{3}{2}}S & 0 & -P-\Delta \end{bmatrix},$$

where

$$\begin{aligned} A &= E_C + A'k^2 + \frac{k^2}{2}, \\ U &= \frac{1}{\sqrt{3}}P_0k_z, \\ V &= \frac{1}{\sqrt{6}}P_0(k_x - ik_y), \\ P &= -E_V + \gamma_1\frac{k^2}{2}, \\ Q &= \gamma_2\frac{1}{2}(k_x^2 + k_y^2 - 2k_z^2), \\ R &= -\frac{\sqrt{3}}{2}[\gamma_2(k_x^2 - k_y^2) - 2i\gamma_3k_xk_y], \\ S &= \sqrt{3}\gamma_3k_z(k_x - ik_y), \end{aligned}$$

In previous equations $|S\rangle$, $|X\rangle$, $|Y\rangle$ and $|Z\rangle$ are the bulk Bloch functions that transform as s , x , y and z under the action of the symmetry group,

$$P_0 = -i\langle S|\hat{p}_x|X\rangle = -i\langle S|\hat{p}_y|Y\rangle = -i\langle S|\hat{p}_z|Z\rangle, \quad (25)$$

is the interband matrix element of the velocity operator [64] usually reported in energy units as $E_P = 2P_0^2$, the parameter A' is related to the conduction band effective mass as

$$A' = \frac{1}{2m^*} - \frac{P_0^2}{E_g + \frac{1}{3}\Delta} - \frac{1}{2}, \quad (26)$$

Δ is the spin-orbit splitting, E_g is the energy gap (the actual energy gap after the effect of Δ was taken into account) equal to $E_g = E_C - E_V$, while

γ_1 , γ_2 and γ_3 are the Luttinger parameters [61] of the 8-band model that can be expressed in terms of the parameters of the 6-band model γ_1^L , γ_2^L and γ_3^L

$$\begin{aligned}\gamma_1 &= \gamma_1^L - \frac{E_P}{3E_g + \Delta}, \\ \gamma_2 &= \gamma_2^L - \frac{1}{2} \frac{E_P}{3E_g + \Delta}, \\ \gamma_3 &= \gamma_3^L - \frac{1}{2} \frac{E_P}{3E_g + \Delta}.\end{aligned}$$

Since material parameters in the Hamiltonian of a quantum dot are position dependent and the \mathbf{k} operators do not commute with coordinate operators, an ambiguity arises about the proper choice of operator ordering. It is necessary to choose the ordering in such a way that the Hamiltonian remains hermitian, however this condition still does not give a unique choice. The most widely used [65, 66, 67, 68, 69] operator ordering in $\mathbf{k} \cdot \mathbf{p}$ -based quantum dot electronic structure calculations is heuristic, symmetrical arrangement of operators

$$\begin{aligned}f(\mathbf{r})k_ik_j &\rightarrow \frac{1}{2} \left(\hat{k}_i f(\mathbf{r}) \hat{k}_j + \hat{k}_j f(\mathbf{r}) \hat{k}_i \right), \\ f(\mathbf{r})k_i &\rightarrow \frac{1}{2} \left(\hat{k}_i f(\mathbf{r}) + f(\mathbf{r}) \hat{k}_i \right).\end{aligned}\tag{27}$$

It has been pointed out that such ordering of operators can lead to unphysical solutions in some circumstances [70]. One can derive the appropriate form of the envelope function Hamiltonian with proper operator ordering starting from the empirical pseudopotential [59] or the LDA Hamiltonian [71], however such Hamiltonians are still not widely used.

A variety of numerical methods can be used to solve the $\mathbf{k} \cdot \mathbf{p}$ Hamiltonian, these include the finite-difference methods [66, 65, 72, 73] and the wavefunction expansion methods, where the basis functions can be plane waves [74, 75, 76, 77, 69, 78], the eigenfunctions of the particle in a cylinder with infinite walls [79, 80, 81] or eigenfunctions of a harmonic oscillator [82].

While the $\mathbf{k} \cdot \mathbf{p}$ model can be quite reliable for large embedded quantum dots, the colloidal quantum dots are often only a few nanometers in size. In reciprocal space, this could correspond to the \mathbf{k} point at 1/3 towards the Brillouin zone boundary, where the $\mathbf{k} \cdot \mathbf{p}$ might no longer be adequate. Indeed, it was found that the $\mathbf{k} \cdot \mathbf{p}$ result compared to the result of a more

accurate calculation might differ by 50% in the confinement energy [83], and sometimes it could change the ordering of the states [84]. Without care, spurious states in the energy gap might appear in $\mathbf{k} \cdot \mathbf{p}$ calculations [85]. These states appear as the consequence of the fact that $\mathbf{k} \cdot \mathbf{p}$ Hamiltonian does not correctly represent the band structure for \mathbf{k} -vectors far away from Γ point and can give states in the gap for these \mathbf{k} -vectors. The finite-difference method is in particular susceptible to the appearance of these states. The wavefunction expansion methods are less susceptible to this [86] since by the expansion in a finite basis set, the high \mathbf{k} components of the envelope function are effectively filtered out. Another issue is that the $\mathbf{k} \cdot \mathbf{p}$ Hamiltonian with a limited number of bands has a larger symmetry group than the true symmetry group of the system. This weakness from the fundamental point of view can be turned into a strength from the computational point of view, as it allows for block diagonalization of the Hamiltonian and therefore a more efficient solution of the problem [87, 81, 77].

2.5 The effect of strain

In previous sections, it was assumed that positions of atoms in a quantum dot are known *a priori* and that local arrangement is the same as in the bulk crystal. However, in real structures this is certainly not the case. Self-assembled quantum dots are grown by depositing layers of material with a different lattice constant than the substrate and therefore the quantum dot is strained. In colloidal quantum dots, there is also some relaxation of atoms close to the surface. It is well understood that strain has a strong effect on the electronic structure of semiconductors. Therefore, in this section, we will describe how can the effect of strain be included in each of the methods described previously.

Within the framework of density functional theory, the effect of strain appears naturally in the formalism itself. One starts with a reasonable initial guess for the positions of atoms in the structure, then self-consistently solves the Kohn-Sham equations and obtains the forces on all atoms. One then moves the atoms in the direction of forces and obtains the new atomic configuration, solves the Kohn-Sham equations again and the whole procedure is repeated until forces become close to zero. In such a way one obtains a new, relaxed configuration for the positions of atoms in the structure. Unfortunately, this procedure is practical only for small systems and is not feasible for larger systems, such as quantum dots.

A widely used methodology to overcome these difficulties is to model the total energy of the system via a classical force field, i.e. to express it as a function of atomic coordinates only. The valence-force field (VFF) model of Keating [88] and Martin [89] is mostly used in inorganic semiconductors for that purpose. Within the VFF model the energy of the system is modeled as [90]

$$\begin{aligned}
E = & \frac{1}{2} \sum_i \sum_j^{nn} \frac{3\alpha_{ij}}{8(d_{ij}^{(0)})^2} \left[(\mathbf{R}_i - \mathbf{R}_j)^2 - (d_{ij}^{(0)})^2 \right]^2 + \\
& \frac{1}{2} \sum_i \sum_{j,k>j}^{nn} \frac{3\beta_{i,jk}}{8d_{ij}^0 d_{ik}^0} \left[(\mathbf{R}_j - \mathbf{R}_i) \cdot (\mathbf{R}_k - \mathbf{R}_i) - \cos \theta_0(jik) d_{ij}^0 d_{ik}^0 \right]^2 \quad (28)
\end{aligned}$$

where d_{ij}^0 are the equilibrium bond lengths between atoms i and j and $\theta_0(jik)$ is the equilibrium angle between bonds ij and ik , which is a constant in zincblende materials ($\theta_0 \approx 109.47^\circ$). In the case of zincblende material, the constants α and β are related to elastic constants of the material via [90]

$$\begin{aligned}
C_{11} + 2C_{12} &= \frac{\sqrt{3}}{4d^0} (3\alpha + \beta) \\
C_{11} - C_{12} &= \frac{\sqrt{3}}{d^0} \beta \\
C_{44} &= \frac{\sqrt{3}}{4d^0} \frac{4\alpha\beta}{\alpha + \beta}
\end{aligned} \quad (29)$$

Although there are three elastic constants and only two parameters α and β , it is possible to choose α and β to fit the C 's of the most zincblende materials within a few percent. To obtain the relaxed atomic structure, one again starts with a reasonable guess for initial atomic structure and then minimizes the expression (28) using some of the standard methods for finding the local minimum of a function, such as the conjugate gradient method. The atomic structure obtained can be used as an input to any of the atomistic approaches previously described: charge patching, empirical pseudopotentials and tight binding.

It has been pointed out in Sec. 2.1. that the charge density motifs used in the charge patching method depend on the local environment of the atom. In strained structures, bond lengths and angles change compared to the ideal ones, which therefore represents the change in the environment that affects the motifs. To include this effect, one introduces so called derivative motifs,

defined as the change in the motif due to a particular bond length or angle change. These motifs can also be extracted from small system calculations on prototype structures with slightly changed bond lengths or angles. After the motifs and derivative motifs are obtained, the total charge density is constructed and the calculation of the electronic structure can be performed as previously described.

It might seem at first sight that it is not necessary to introduce any modifications to the empirical pseudopotential Hamiltonian to include the effects of strain. However, it turns out that within such an approach it would be difficult to correctly describe the dependence of the valence band maximum state on the hydrostatic strain [91]. Therefore, a strain-dependent term is introduced for the local part of the pseudopotential of the atom of type α in the form:

$$v_{\alpha}^{loc}(\mathbf{r}, e) = v_{\alpha}^{loc}(\mathbf{r}, 0) [1 + \gamma_{\alpha} \text{Tr}(e)], \quad (30)$$

where γ_{α} is a fitting parameter and $\text{Tr}(e) = e_{xx} + e_{yy} + e_{zz}$ is the trace of the strain tensor. The SEPM strain-dependent Hamiltonian obtained this way can be solved either by representing it in the basis of plane waves or bulk Bloch bands. The extension of the unstrained cases to the strained cases for the basis of plane waves is straightforward. On the other hand, this is not true if bulk Bloch bands are used since the Bloch functions of the unrelaxed system form a poor basis set for the relaxed system. Therefore one needs to use the "strained" linear combination of Bloch bands and the method is then referred to as the SLCBB method. The reader is referred to Ref. [48] for technical details of the implementation of the SLCBB method.

The natural way to introduce strain in tight-binding models is via the dependence of hopping integrals on bond lengths and bond angles. The dependence on bond lengths is modeled by scaling the Slater-Koster two-center integrals [49] from which the hopping integrals are constructed as

$$V = V_0 \left(\frac{d_0}{d} \right)^{\eta}, \quad (31)$$

which is a generalization [52, 92] of Harrison's d^{-2} rule [56, 50]. In the above equation V_0 is the integral for equilibrium bond length d_0 and V the integral when the bond length is d . The change in bond angles in the system leads to different relative orientation of orbitals of neighboring atoms and consequently to a different hopping integral. This effect is naturally included through the Slater-Koster [49] tables of matrix elements in terms

of the two-center integrals and direction cosines. Furthermore, there is a question whether the influence of strain on onsite energies should also be included. This is indeed done in many recent works [93, 92, 94], although different methods are used. Currently, there does not seem to exist a unique and simple model for the inclusion of this dependence as for the hopping integrals.

In $\mathbf{k} \cdot \mathbf{p}$ models the effect of strain is included through the bulk deformation potential parameters that can be either measured or determined from *ab-initio* calculations. In the case of 8-band Hamiltonian for zincblende crystals the strain contribution to the Hamiltonian reads

$$\hat{H}_s = \begin{matrix} & & & & & & & (32) \\ \left[\begin{array}{cccccccc} a_c e & 0 & -v^+ & 0 & -\sqrt{3}v & \sqrt{2}u & u & -\sqrt{2}v^+ \\ 0 & a_c e & \sqrt{2}u & \sqrt{3}v^+ & 0 & v & -\sqrt{2}v & -u \\ -v & \sqrt{2}u & -p+q & -s^+ & r & 0 & \sqrt{\frac{3}{2}}s & -\sqrt{2}q \\ 0 & \sqrt{3}v & -s & -p-q & 0 & r & -\sqrt{2}r & \frac{1}{\sqrt{2}}s \\ -\sqrt{3}v^+ & 0 & r^+ & 0 & -p-q & s^+ & \frac{1}{\sqrt{2}}s^+ & \sqrt{2}r^+ \\ \sqrt{2}u & v^+ & 0 & r^+ & s & -p+q & \sqrt{2}q & \sqrt{\frac{3}{2}}s^+ \\ u & -\sqrt{2}v^+ & \sqrt{\frac{3}{2}}s^+ & -\sqrt{2}r^+ & \frac{1}{\sqrt{2}}s & \sqrt{2}q & -p & 0 \\ -\sqrt{2}v & -u & -\sqrt{2}q & \frac{1}{\sqrt{2}}s^+ & \sqrt{2}r & \sqrt{\frac{3}{2}}s & 0 & -p \end{array} \right], \end{matrix}$$

where

$$\begin{aligned} e &= e_{11} + e_{22} + e_{33}, \\ p &= a_v e, \\ q &= b \left[e_{33} - \frac{1}{2}(e_{11} + e_{22}) \right], \\ r &= \frac{\sqrt{3}}{2} b (e_{11} - e_{22}) - i d e_{12}, \\ s &= -d (e_{13} - i e_{23}), \\ u &= \frac{1}{\sqrt{3}} P_0 \sum_{j=1}^3 e_{3j} k_j, \\ v &= \frac{1}{\sqrt{6}} P_0 \sum_{j=1}^3 (e_{1j} - i e_{2j}) k_j, \end{aligned}$$

where a_c and a_v are the conduction and valence band hydrostatic deformation potentials, respectively, b and d are the shear deformation potentials.

The strain tensor that enters the Hamiltonian (32) can be obtained either from the VFF model (previously described) or from continuum mechanical (CM) model.

In the CM model, the quantum dot structure is modelled by an elastic classical continuum medium whose elastic energy is given by

$$W = \frac{1}{2} \sum_{ijkl} \int d^3\mathbf{r} \lambda_{ijkl} e_{ij} e_{kl}, \quad (33)$$

where λ_{ijkl} is the elastic tensor relating the stress and strain tensor by Hooke's law

$$\sigma_{ij} = \sum_{kl} \lambda_{ijkl} e_{kl}. \quad (34)$$

In the crystals with zincblende lattice the elastic tensor is of the form

$$\lambda_{ijkl} = C_{12} \delta_{ij} \delta_{kl} + C_{44} (\delta_{ik} \delta_{jl} + \delta_{il} \delta_{jk}) + C_{an} \sum_{p=1}^3 \delta_{ip} \delta_{jp} \delta_{kp} \delta_{lp}, \quad (35)$$

where C_{12} , C_{44} and $C_{an} = C_{11} - C_{12} - 2C_{44}$ are the elastic constants. The finite element discretization and minimization of the functional (33) leads to a system of linear equations that can be efficiently solved.

There have been several comparisons in the literature between the VFF and CM models [66, 90, 95]. While certain differences have been obtained, the results of the two models give overall agreement, as can be seen from a comparison between strain distribution in a pyramidal InAs/GaAs quantum dot from Ref. [90] that is given in Fig. 1. From the fundamental point of view, the advantage of the VFF model is that it captures the atomistic symmetry of the system, while CM models have a higher symmetry group. From the computational point of view, the VFF model is more demanding as the displacement of each atom is considered, in contrast to CM models where a grid of the size of lattice constant or even larger may be used, leading to a smaller number of variables to be handled. In several important cases, there are analytical or nearly analytical solutions of the CM model [96, 97]. However, these advantages of the CM models are becoming less important as modern computers can handle the VFF calculations quite easily.

The non-self-consistent methods described above do not allow for long ranged charge redistributions and therefore neglect the effects such as piezoelectricity where charge is moved due to strain. The piezoelectric potential then has to be calculated independently and added as an additional potential. The components of piezoelectric polarization in a crystal of arbitrary

symmetry are given as

$$P_i = \sum_{k,l=1}^3 \epsilon_{ikl} e_{kl}, \quad (36)$$

where ϵ_{ikl} are the piezoelectric constants of the material. In a crystal with zincblende symmetry, the only nonzero components of ϵ_{ikl} are

$$\epsilon_{123} = \epsilon_{132} = \epsilon_{213} = \epsilon_{231} = \epsilon_{312} = \epsilon_{321}, \quad (37)$$

The charges induced by piezoelectric polarization can then be calculated and the additional piezoelectric potential is obtained from the solution of Poisson equation. It has been recently realized that in addition to the first order piezoelectric effect given by Eq. 36, second order piezoelectric effects might be important as well [98].

3. MANY-BODY APPROACHES

The methods presented in Sec. 2 give a strategy for calculating the single particle states. These can be very useful for calculating the optical properties, as will be demonstrated for example in Sec 4.3. Nevertheless, there are cases when the many-body nature of electron-hole excitations should be directly considered. The approaches along this line will be described in Sec. 3.

3.1 Time dependent density functional theory

Within the time dependent DFT (TDDFT) [99, 100], one solves the time dependent Kohn-Sham equations:

$$i \frac{\partial}{\partial t} \psi_i(\mathbf{r}, t) = \left[-\frac{1}{2} \nabla^2 + V(\mathbf{r}, t) \right] \psi_i(\mathbf{r}, t), \quad (38)$$

where

$$\rho(\mathbf{r}, t) = \sum_{i=1}^M |\psi_i(\mathbf{r}, t)|^2 \quad (39)$$

The potential $V(\mathbf{r}, t)$ should depend in principle on charge density in all times before t . A widely used approximation is the adiabatic LDA, in which it is assumed that $V(\mathbf{r}, t)$ depends only on $\rho(\mathbf{r}, t)$ and that the functional form of this dependence is the same as in LDA in time independent DFT. We will refer to this approximation as time dependent LDA (TDLDA).

The TDLDA can be used to calculate the optical absorption spectrum by adding the external electromagnetic field perturbation potential to Eq. 38 and solving the equations by explicit integration in time [101]. Another approach is to assume that the perturbation is small and use the linear response theory. The exciton energy can then be found from the eigenvalue problem

$$\sum_{jl} [(\epsilon_i - \epsilon_k)\delta_{ij}\delta_{kl} + (f_i - f_k)K_{ik,jl}(\omega)]C_{jl} = \omega C_{ik}, \quad (40)$$

where ϵ_i and ϵ_k are the LDA ground state Kohn-Sham eigen energies, and f_i and f_k are the occupation number of Kohn-Sham eigen states ψ_i and ψ_k . Within TDLDA, $K_{ik,jl}$ becomes independent of ω and is given as:

$$K_{ik,jl} = \int \int d\mathbf{r}_1 d\mathbf{r}_2 \psi_i(\mathbf{r}_1) \psi_k(\mathbf{r}_1) \left[\frac{1}{|\mathbf{r}_1 - \mathbf{r}_2|} + \delta(\mathbf{r}_1 - \mathbf{r}_2) \frac{\partial \mu_{xc}^{LDA}(\rho(\mathbf{r}_1))}{\partial \rho(\mathbf{r}_1)} \right] \psi_j(\mathbf{r}_2) \psi_l(\mathbf{r}_2), \quad (41)$$

where $\mu_{xc}^{LDA}(\rho)$ is the LDA exchange-correlation potential. The first term in Eq. 41 is the exchange interaction, while the second can be called the screened Coulomb interaction. The justification of this assignment would require a comparison with equations from other approaches, such as the configuration interaction and GW + Bethe Salpeter equation. It might also seem surprising that the screened Coulomb interaction is not a nonlocal integral between \mathbf{r}_1 and \mathbf{r}_2 . This is because in the LDA, the exchange-correlation term is a local functional of charge density.

TDLDA appears to work quite well for optical spectra of small clusters and molecules. The results of TDLDA can then agree quite well with experimental measurements, as shown for example for the case of SiH_4 in [102]. These results are significantly improved compared to bare LDA results, which is due to exchange interaction in Eq. 40, which can be quite strong in such small systems. The screened Coulomb interaction in Eq. 40, however, does not play a significant role then, as also shown in [102].

On the other hand the TDLDA is not as accurate for larger systems. For bulk system, it is known that [103, 104] the TDLDA band gap will be the same as the LDA band gap. The TDLDA does not provide a better bulk optical absorption spectrum than the LDA, as shown in [102]. The origin of these problems is the screened Coulomb interaction in Eq. 40, which gives a significant contribution then. However, such diagonal form of

screened Coulomb interaction is not able to correctly describe its long range behavior.

Density functionals other than the LDA can also be used in conjunction with TDDFT. A very popular approach is to use the hybrid B3LYP functional [105]. Within the B3LYP approach, the total energy is modeled as a linear combination of the exact Hartree-Fock exchange with local and gradient-corrected exchange and correlation terms. The coefficients in the linear combination were chosen to fit the properties of many small molecules. The B3LYP method gives accurate band gaps for various bulk crystals [106]. Since it contains the explicit exchange integral, it introduces the long range Coulomb interaction in Eq. 40. Therefore, the TDDFT-B3LYP can overcome the two difficulties of TDLDA previously discussed.

3.2 Configuration interaction method

When the single particle states are obtained, one can form many body excitations by creating Slater determinants out of these single particle states. One can then diagonalize the many body Hamiltonian in the Hilbert space formed from a restricted set of such determinants. This approach is called the configuration interaction (CI) method. When one is interested in excitons, the wavefunction is assumed as

$$\Psi = \sum_{v=1}^{N_v} \sum_{c=1}^{N_c} C_{v,c} \Phi_{v,c}, \quad (42)$$

where $\Phi_{v,c}$ is the Slater determinant when the electron from the valence band state v is excited to the conduction band state c . The eigenvalue problem of the Hamiltonian then reads

$$\sum_{v'c'} H_{vc,v'c'} C_{v'c'} = \sum_{v'c'} [(E_v - E_c) \delta_{v,v'} \delta_{c,c'} + K_{vc,v'c'} - J_{vc,v'c'}] C_{v'c'} = E C_{vc}, \quad (43)$$

where E_v and E_c are the single particle eigen energies, E is the exciton energy and $K_{vc,v'c'}$ and $J_{vc,v'c'}$ are the exchange and Coulomb interactions respectively:

$$K_{vc,v'c'} = \int \int \frac{\psi_{c'}(\mathbf{r}_1) \psi_{v'}^*(\mathbf{r}_1) \psi_v(\mathbf{r}_2) \psi_c^*(\mathbf{r}_2)}{\bar{\epsilon}(\mathbf{r}_1, \mathbf{r}_2) |\mathbf{r}_1 - \mathbf{r}_2|} d\mathbf{r}_1 d\mathbf{r}_2 \quad (44)$$

$$J_{vc,v'c'} = \int \int \frac{\psi_v(\mathbf{r}_1) \psi_{v'}^*(\mathbf{r}_1) \psi_{c'}(\mathbf{r}_2) \psi_c^*(\mathbf{r}_2)}{\bar{\epsilon}(\mathbf{r}_1, \mathbf{r}_2) |\mathbf{r}_1 - \mathbf{r}_2|} d\mathbf{r}_1 d\mathbf{r}_2 \quad (45)$$

The effective dielectric screening used in Eqs. 44 and 45 is of the form

$$\frac{1}{\bar{\epsilon}(\mathbf{r}_1, \mathbf{r}_2)|\mathbf{r}_1 - \mathbf{r}_2|} = \int \epsilon_{bulk}^{-1}(\mathbf{r}_1, \mathbf{r}) \frac{1}{|\mathbf{r} - \mathbf{r}_2|} d\mathbf{r}, \quad (46)$$

where $\epsilon_{bulk}^{-1}(\mathbf{r}_1, \mathbf{r})$ is the bulk inverse dielectric function that differs from the one of the quantum dot nanostructure, which also contains the surface polarization potential P discussed in Sec. 2. The use of bulk inverse dielectric function is in line with the fact that the single particle energies E_c and E_v are obtained from the Schrödinger's equation that does not contain the surface polarization term. If the surface polarization term is used in the single particle equation, then the full inverse dielectric function should be used and the surface polarization terms will roughly cancel out.

There are arguments that the exchange interaction $K_{vc,v'c'}$ should not be screened, that come from the two particle Green's function construction, where screening of the exchange term would cause double counting [107]. Nevertheless, in practice, it is found that the exchange consists of a long range term, that should be unscreened, and a short range term [108] that should be screened by the bulk dielectric function [109, 110]. The effective dielectric function $\bar{\epsilon}(\mathbf{r}_1, \mathbf{r}_2)$ used in Eq. 44 incorporates this because $\bar{\epsilon}(\mathbf{r}_1, \mathbf{r}_2) \rightarrow 1$ for $|\mathbf{r}_1 - \mathbf{r}_2| \rightarrow 0$. The seeming contradiction to the Green's function argument can be resolved by realizing that if only a limited configuration space is used in Eq. 43, the effect of other unused configurations can be included in the exchange screening term [107].

The CI equation 43 has the same form as the corresponding equation in TDLDA (Eq.40), with the difference in the expressions for the exchange and the Coulomb integrals. On top of a single particle calculation, the CI method was used to calculate very large systems, such as pyramidal quantum dots with near one million atoms [111]. It was also used to calculate many body excitations, such as multiexcitons, few electron excitations and to study Auger effects [112]. All these calculations are made possible by selecting a limited window of single-particle states used in these configurations. It is difficult or impossible to study such systems using TDLDA or GW+Bethe-Salpeter equation. One should nevertheless be cautious about the models used for screening in these multi-particle excitations.

3.3 GW and Bethe-Salpeter equation approach

Within this approach, one first calculates the quasiparticle eigenenergies, which is somewhat analogous to single particle calculations in Sec. 2. These

are then used to solve the Bethe-Salpeter equation (BSE) for excitons, which is in some sense similar to CI equations of the previous section.

A quasiparticle is defined as the pole in frequency space in the single particle Green's function:

$$G(\mathbf{r}t, \mathbf{r}'t') = -i\langle M|T\hat{\psi}(\mathbf{r}t)\hat{\psi}^\dagger(\mathbf{r}'t')|M\rangle \quad (47)$$

where $\hat{\psi}(\mathbf{r}t)$ is the particle creation operator, $|M\rangle$ is the M particle ground state, and T is the time-ordering operator. Quasiparticle energies correspond to energies for adding or removing one electron from the system [113]. Within the GW approximation [114] the appropriate single-particle equation reads:

$$\begin{aligned} & \left[-\frac{1}{2}\nabla^2 + \sum_{atom} \hat{v}_{bare}(\mathbf{r} - \mathbf{R}_{atom}) + \int \frac{\rho(\mathbf{r}')}{|\mathbf{r} - \mathbf{r}'|} d^3\mathbf{r}' \right] \psi_i(\mathbf{r}) \\ & + \int \Sigma(\mathbf{r}, \mathbf{r}'; \epsilon_i) \psi_i(\mathbf{r}') d\mathbf{r}' = \epsilon_i \psi(\mathbf{r}), \end{aligned} \quad (48)$$

where

$$\Sigma(\mathbf{r}, \mathbf{r}', \omega) = -\sum_k \psi_k(\mathbf{r}) \psi_k^*(\mathbf{r}') [f_k W(\mathbf{r}, \mathbf{r}', \epsilon_k - \omega) + \frac{1}{\pi} \int \frac{\text{Im}W(\mathbf{r}, \mathbf{r}', \omega')}{\omega - \epsilon_k - \omega' + i\delta} d\omega'] \quad (49)$$

is the self-energy potential that replaces the LDA exchange correlation potential of LDA single particle equations.

$$W(\mathbf{r}, \mathbf{r}', \omega) = \int \epsilon^{-1}(\mathbf{r}, \mathbf{r}_1, \omega) \frac{1}{|\mathbf{r}_1 - \mathbf{r}'|} d\mathbf{r}_1 \quad (50)$$

is the dynamically screened interaction, where $\epsilon^{-1}(\mathbf{r}, \mathbf{r}_1, \omega)$ is the inverse dielectric function.

While Eqs. 48 and 49 should in principle be solved self-consistently, one usually replaces the self-energy term with its expectation value with respect to the LDA Kohn-Sham wavefunctions $\langle \psi_k | \Sigma | \psi_k \rangle$, which constitutes the zero-th order approximation of the GW procedure. It has been shown that the self-consistent calculations [115, 116, 117, 118, 119] make the spectral properties worse. Such calculations are performed with the use of pseudopotentials. It is possible that self-consistency will not make the results worse if all-electron calculation is performed.

The two particle Green's function defined as

$$G(\mathbf{r}_1 t_1, \mathbf{r}_2 t_2, \mathbf{r}'_1 t'_1, \mathbf{r}'_2 t'_2) = -\langle M|T\psi(\mathbf{r}_1 t_1)\psi(\mathbf{r}_2 t_2)\psi^\dagger(\mathbf{r}'_2 t'_2)\psi^\dagger(\mathbf{r}'_1 t'_1)|M\rangle \quad (51)$$

contains the information about the exciton energies. These can be retrieved by taking $t_1 = t'_1 + 0^-$, $t_2 = t'_2 + 0^-$ and transforming to frequency space to obtain (in the condensed notation) $G_2(\omega)$, whose poles are the exciton energies. The Dyson equation for $G_2(\omega)$ reads [120, 113]

$$G_2(\omega) = G_2^{(0)}(\omega) + G_2^{(0)}(\omega)K'(\omega)G_2(\omega) \quad (52)$$

where $G_2^{(0)}(\omega)$ is the non-interacting two particle Green's function, and $K'(\omega)$ is an electron-hole interaction kernel. Equation 52 for the electron-hole pair is called the Bethe-Salpeter equation [120]. It can be solved by expanding the exciton wavefunction as

$$|M, S\rangle = \sum_v \sum_c C_{vc} \hat{a}_v^\dagger \hat{b}_c^\dagger |M, 0\rangle. \quad (53)$$

The equation for C_{vc} coefficients are then given as

$$(\epsilon_c - \epsilon_v)C_{vc} + \sum_{v'c'} (K_{vc,v'c'} - J_{vc,v'c'})C_{v'c'} = \Omega_S C_{vc} \quad (54)$$

where ϵ_n , ϵ_m are the quasi-particle eigen energies obtained from Eq. 48, and Ω_S is the exciton energy. The $K_{vc,v'c'}$ is the same as in Eq. 44 without the screening $\bar{\epsilon}(\mathbf{r}_1, \mathbf{r}_2)$. The $J_{vc,v'c'}$ on the other hand reads

$$J_{vc,v'c'} = \int d\mathbf{r} d\mathbf{r}' \psi_c^*(\mathbf{r}) \psi_{c'}(\mathbf{r}) \psi_v(\mathbf{r}') \psi_{v'}^*(\mathbf{r}') \frac{i}{2\pi} \int d\omega e^{-i\omega 0^+} W(\mathbf{r}, \mathbf{r}', \omega) \\ \times [(\Omega_S - \omega - (\epsilon_{c'} - \epsilon_v) + i0^+)^{-1} + (\Omega_S + \omega - (\epsilon_c - \epsilon_{v'}) + i0^+)^{-1}] \quad (55)$$

where $W(\mathbf{r}, \mathbf{r}', \omega)$ is the screened Coulomb interaction given by Eq. 50.

GW + BSE approach is thought to be one of the most reliable methods for the calculation of the optical absorption spectra and excited state electronic structures. It has been used to calculate small molecules and bulk crystals. Unfortunately, its use for the larger systems is hindered by the significant computational cost.

Excellent agreement with experimental results was obtained for the optical absorption spectrum of bulk Si calculated using the GW + BSE approach [121]. Within GW + BSE, the lower energy peak originating from the excitonic binding effect was obtained for the first time. In contrast, previous LDA and TDLDA results were unable to predict this peak due to the inadequacy of the local approximation for the Coulomb interaction.

The BSE (Eq. 54) is formally the same as the linear response TDLDA (Eq. 40) and CI (Eq. 43), except for the meanings of single-particle energies

and the exchange and screened Coulomb interaction. In the GW + BSE approach, the quasiparticle electron (hole) energies are equal to the total energy difference for adding (removing) one electron from the system and include the surface polarization term $P(\mathbf{r})$ from Eq. 1. On the other hand, in the CI approach, the single particle states are obtained without including the $P(\mathbf{r})$ term. The single particle states then do not correspond to total energy differences for adding or removing one electron. A surface polarization term needs to be added to relate them to ionization energies or electron affinities [122]. In the linear response TDLDA Eq. 40, the single particle energy is the Kohn-Sham LDA eigenenergy. It does not contain the surface polarization term, just like the single particle energies in the CI approach. A difference between the TDLDA and CI approach is that TDLDA contains LDA band gap error, while in the CI approach the single particle states can be found for example by EPM or SEPM that correct the LDA band gap error.

The polarization term in the GW quasiparticle eigenenergy cancels out a term in J in Eq. 54 because the same surface polarization term exists in $W(\mathbf{r}, \mathbf{r}', \omega)$ in Eq. 55. This cancellation corresponds to the cancellation of the $P_M(\mathbf{r}_1, \mathbf{r}_2)$ and $P(\mathbf{r}_1), P(\mathbf{r}_2)$ terms in Eq. 2 of the classical phenomenological analysis. Delerue, Lannoo and Allan [123] have shown numerically that the Coulomb correction term cancels the polarization term in the self-energy of the quasi-particle eigenenergy. Consequently the results of the GW BSE are expected to be similar to the results of CI where J is screened by the bulk dielectric function. In the TDLDA, where the Coulomb interaction is local, it is also screened by the bulk dielectric function, in line with the fact the LDA single particle states used in Eq. 40 do not include the surface polarization term. The different cancellation schemes in TDLDA, CI and GW BSE (Eqs. 40, 43 and 54) can be illustrated by comparing the calculated absorption spectra in these methods with the one obtained from single particle energies. It was shown in [124] that the BSE absorption spectrum of small clusters of Si_nH_m is red shifted from the calculated single particle spectrum, which is mostly due to negative surface polarization energies in the Coulomb interaction J . On the other hand it was shown in [102], that the TDLDA spectrum is blue shifted from the single particle LDA spectrum. There is no surface polarization in J or single particle energies then, thus the exchange interaction dominates the spectrum shift. However, if total LDA energy differences for adding or removing an electron are used in Eq.40, then the surface polarization must be considered [125] and Coulomb interaction cannot be calculated from Eqs. 45 and 46. The above discussed cancellations are only good for spherical quantum dots. For quantum rods,

wires and the nanostructures of other shapes, the GW BSE-like approach should be used. In the CI approach, $P(\mathbf{r})$ should be added to the single particle energy, while the full nanosystem inverse dielectric function (not the bulk one) should be used for $\bar{\epsilon}(\mathbf{r}_1, \mathbf{r}_2)$ in Eqs. 44 and 45.

3.4 Quantum Monte Carlo Methods

Within the quantum Monte Carlo (QMC) method [126], the whole system is described by a many-body wavefunction and the many body Schrödinger equation is solved using some of the Monte Carlo techniques such as variational quantum Monte Carlo method [127, 128] (VMC) or diffusion quantum Monte Carlo method [129, 130] (DMC).

Within the VMC, the variational form of the many body wavefunction $\Psi(\mathbf{X})$ is assumed as a Slater determinant multiplied by a Jastrow term:

$$\Psi(\mathbf{X}) = D^\dagger(\mathbf{R})D^\dagger(\mathbf{R}) \exp \left[\sum_{i=1}^M \chi(\mathbf{r}_i) - \sum_{i<j}^M u(|\mathbf{r}_i - \mathbf{r}_j|) \right] \quad (56)$$

where $\mathbf{X} = \{\mathbf{r}_i, s_i\}$ for $i = 1, M$. The Slater determinant D is usually constructed from single particle LDA or Hartree Fock wavefunctions, while parameterized forms are used to express χ and u . The total energy of the system is found by minimizing the expectation value of the many body Hamiltonian H , given as

$$E = \langle \Psi | H | \Psi \rangle / \langle \Psi | \Psi \rangle.$$

The last expression can be rewritten as

$$E = \frac{\int \Psi(\mathbf{X}) H \Psi(\mathbf{X}) d\mathbf{X}}{\int |\Psi(\mathbf{X})|^2 d\mathbf{X}} = \frac{\int \left[\frac{H\Psi(\mathbf{X})}{\Psi(\mathbf{X})} \right] |\Psi(\mathbf{X})|^2 d\mathbf{X}}{\int |\Psi(\mathbf{X})|^2 d\mathbf{X}} \quad (57)$$

The last integral can be viewed as the average value of the quantity $\frac{H\Psi(\mathbf{X})}{\Psi(\mathbf{X})}$ distributed in multidimensional space with a probability $|\Psi(\mathbf{X})|^2$. It can be found using the Metropolis algorithm. In this algorithm, one simulates the path of the walker in the multidimensional space. The jump of the walker from \mathbf{X} to \mathbf{X}' is accepted if $\mu = |\Psi(\mathbf{X}')|^2 / |\Psi(\mathbf{X})|^2 > 1$ and accepted with probability μ if $\mu < 1$. The average value of $\frac{H\Psi(\mathbf{X})}{\Psi(\mathbf{X})}$ along the path of the walker gives E in Eq. 57.

In the DMC, one treats the many body imaginary time Schrödinger equation as the classical diffusion equation [129, 130]. In this method, the many

body wave function (not its square) corresponds to the equilibrium distribution of Monte Carlo walkers. However, for fermion system, antisymmetry is required for the many body wavefunction. This causes a sign problem, which is usually approximately solved by a fixed nodal approximation where an auxiliary wavefunction is used to define the fixed nodal hypersurface for the DMC wavefunction. Usually, the VMC wavefunction of Eq. 56 is used as this auxiliary wavefunction.

With the use of pseudopotentials [131], both VMC and DMC methods have been used for systems up to a dozen atoms. Williamson *et al* [132] showed that QMC methods can be used for exciton energies. This is done by replacing one single particle valence band wave function with a conduction band wave function in the Slater determinant. The DMC with a nodal hypersurface defined by this new Slater determinant is performed then, and it fully takes into account the resulting correlation effects. This approach gives the Si band structure that agrees well with the experiments. QMC is one of the most reliable methods for small system calculations.

The development of a linear scaling QMC method [133] extended its applicability from a dozen atoms to a few hundred atoms. Within the linear scaling QMC method, Slater determinants are represented in a basis of localized Wannier functions. This makes the Slater determinant sparse and therefore the calculation time is proportional to the size N , instead of N^3 in the old scheme. Consequently, this allows the QMC calculation of a few hundred atoms, and makes possible the use of the QMC method for small quantum dots [134].

4. APPLICATION TO DIFFERENT PHYSICAL EFFECTS: some examples

4.1 Electron and hole wave functions

The shape of the single particle wave functions and their energies determine many physical properties of quantum dots. This section is therefore devoted to the analysis of electron and hole wave functions. The wave functions of the lowest four states in the conduction band and top four states in the valence band of a pyramidal [110]-faceted InAs/GaAs quantum dot are presented in Fig. 2. The results presented in Fig. 2 were obtained using the empirical pseudopotential method, including the effect of spin-orbit

interaction.

The lowest conduction state is an s -like state, while the next two conduction states are p -like states oriented in the directions of base diagonals, with nodal planes perpendicular to these directions. These are followed by d -like states. Due to lateral dimension larger than the quantum dot height, none of the nodal planes is parallel to the pyramid base. There are therefore only two p -like states, in contrast to spherical quantum dots where there are three p -like states.

The two p -states are relatively close in energy and their splitting is caused by several effects. To discuss each of these effects, we first assume that the structure is unstrained.

(1) In the simplest single band effective mass model these states are degenerate and can be split if the base of the pyramid acquires a shape different than the square. The same is the case for the 4-band $\mathbf{k} \cdot \mathbf{p}$ model (i.e. 8-band model without spin-orbit effects). Addition of spin-orbit effects to 4-band $\mathbf{k} \cdot \mathbf{p}$ splits these levels by a small (less than 1 meV) amount [77, 135]. Atomistic methods predict the correct symmetry of the system and split the p -states, as well as $\mathbf{k} \cdot \mathbf{p}$ models with larger number of bands (14 for example).

(2) When strain (without piezoelectricity) is included in the $\mathbf{k} \cdot \mathbf{p}$ model within CM approach, it cannot cause the splitting, while the VFF model, due to its atomistic nature, splits the p -states.

(3) Piezoelectricity added to any of the models also causes the splitting of the p -states.

The splitting of the p -states is therefore caused by the shape anisotropy, spin-orbit effect, atomistic (a)symmetry, strain and piezoelectricity. It is amazing that a single quantity is determined by such a large number of effects. Unfortunately in a given quantum dot, all these effects are present and cannot be probed separately.

The conduction band states are formed essentially of a single envelope function and therefore these can be classified as being s , p , d -like. On the other hand, the band mixing of the valence states is much stronger and such a simple classification is not possible. The valence band functions actually have no nodal planes. (This becomes obvious from Fig. 2, when the isosurface values are additionally reduced for VBM-1 and VBM-2). The approximation of using a single heavy hole band to describe the valence state, which is often used in quantum wells is therefore not applicable to quantum dots due to stronger heavy and light hole mixing.

As the dot size is reduced, the valence band energies become lower and

the conduction band energies higher. The bound states are then less confined and the effective energy gap increases. With the reduction in quantum dot dimensions some bound states become mixed with wetting layer or continuum states and the number of truly bound states decreases.

4.2 Intraband optical processes in embedded quantum dots

Most of the semiconductor optoelectronic devices utilize transitions between the conduction band states and the valence band states. The operating wavelength of these devices is mainly determined by the bandgap of the materials employed and is therefore limited to the near-infrared and visible part of the spectrum. However, if one wishes to access longer wavelengths, a different approach is necessary, i.e. the transitions within the same band have to be used. These transitions are called intraband transitions. Intraband optical transitions in bulk are not allowed and therefore low dimensional nanostructures have to be used. Therefore, in the last two decades, semiconductor nanostructures, such as quantum wells, wires and dots have been recognized as sources and detectors of electromagnetic radiation in the mid- and far-infrared region of the spectrum.

When the use of nanostructures as detectors is concerned, several limitations of quantum well infrared photodetectors (QWIPs) have motivated the development of quantum dot infrared photodetectors (QDIPs). The main origin of the undesirable dark current in QWIPs is thermal excitation (due to interaction with phonons) of carriers from the ground state to continuum states. The discrete electronic spectrum of quantum dots as opposed to continuum spectrum of quantum wells significantly reduces the phase space for such processes and therefore reduces the dark current. Higher operating temperatures of QDIPs are therefore expected. Due to optical selection rules, QWIPs based on intersubband transitions in the conduction band interact only with radiation having the polarization vector in the growth direction. This is not the case in quantum dots since these are three dimensional objects where the corresponding selection rules are different.

For the QDIP applications, it is essential to understand the quantum dot absorption spectrum. The simplest model which is sufficient to qualitatively understand the quantum dot intraband absorption spectrum is the parabolic dot model, where the potential is assumed in a separable form $V(\mathbf{r}) = V_1(x, y) + V_2(z)$, where $V_1(x, y) = \frac{1}{2}m^*\omega^2(x^2 + y^2)$ is the potential of a two dimensional harmonic oscillator, and $V_2(z)$ is the po-

tential of a quantum well confining the electrons in the z -direction. The solutions are of the form $\Psi(\mathbf{r}) = h_{n_x}(x)h_{n_y}(y)\psi_{n_z}(z)$, where $h_n(t)$ is the wavefunction of an one dimensional harmonic oscillator and $\psi_{n_z}(z)$ are solutions of the one dimensional Schrödinger equation with potential $V_2(z)$ (corresponding to energies ε_{n_z}). The eigenenergies are then of the form $E(n_x, n_y, n_z) = \hbar\omega(n_x + n_y + 1) + \varepsilon_{n_z}$. The factor $\hbar\omega$ corresponds to the transition energy from the ground to first excited state and for modelling realistic quantum dots it should be set to $\hbar\omega \sim 40 - 70$ meV. Typical quantum dots are wide in the xy -plane (diameters of the order of 20 nm and more) and have very small height (of the order of 3-7 nm) in the z -direction, therefore the effective potential well representing the z -direction confinement is narrow (see Fig. 3). In a typical case therefore $\varepsilon_1 - \varepsilon_0$ is of the order of at least 100 meV.

The optical absorption matrix elements on the transitions between states are proportional to the matrix elements of coordinate operators, therefore by calculating the latter, one obtains the following selection rules on the transitions between states:

- $\Delta n_x = \pm 1, \Delta n_y = 0, \Delta n_z = 0$, for x -polarized radiation,
- $\Delta n_y = \pm 1, \Delta n_x = 0, \Delta n_z = 0$, for y -polarized radiation,
- $\Delta n_x = 0, \Delta n_y = 0$, for z -polarized radiation.

The transitions from the ground state are of primary importance for QDIPs. From the selection rules obtained, one concludes that only the transition to a pair of degenerate first excited states is allowed for in-plane polarized radiation, while in the case of z -polarized radiation, only the transitions to higher excited states are allowed, as demonstrated in Fig. 3.

Although the model presented considers the quantum dot bandstructure in a very simplified manner, it is excellent for understanding the results of more realistic models. The strict selection rules from this model are then relaxed and strictly forbidden transitions become weakly allowed. Nevertheless, qualitatively, the absorption spectrum retains the same features as in this model.

The absorption spectrum obtained by the 8-band $\mathbf{k} \cdot \mathbf{p}$ model for a quantum dot of conical shape with the diameter $D = 25$ nm and height $h = 7$ nm, is presented in Fig. 4. The dimensions were chosen to approximately match those reported for quantum dots in a QDIP structure in Ref. [136]. The optical absorption spectrum in the case of z -polarized radiation is shown

in Fig. 4a. The experimental intraband photocurrent spectrum exhibits the main peak at 175 meV and a much smaller peak at 115 meV, in excellent agreement with the results obtained for z -polarized incident radiation where the corresponding peaks occur at 179 meV and 114 meV, respectively. The corresponding absorption spectrum for in-plane polarized incident radiation is presented in the inset of Fig. 4a. There is a single peak in the spectrum which is due to the transition from the ground state to a pair of nearly degenerate first excited states (see Fig. 4b).

The results presented and other similar calculations suggest that the in-plane polarized radiation causes non-negligible transitions only between the ground and first excited state, these being located in the region 40–80 meV in the far-infrared. On the other hand, z -polarized radiation causes the transition in the $\sim 100 - 300$ meV region in the mid-infrared. The best way to understand the origin of such behavior is via a simplified parabolic model presented. Such behavior can be altered only if the dot dimension in the z -direction becomes comparable to the in-plane dimensions.

4.3 Size dependence of the band gap in colloidal quantum dots

The size dependence of the bandgap is the most prominent effect of quantum confinement in semiconductor nanostructures. The bandgap increases as the nanostructure size decreases. Many of quantum dot applications rely on the size dependence of the optical properties. Therefore studying the size dependence of the band gap is one of the most important topics in semiconductor nanocrystal research.

According to a simple effective-mass approximation model, the band gap increase of spherical quantum dots from the bulk value is

$$\Delta E_g = \frac{2\hbar^2\pi^2}{m^*d^2}, \quad (58)$$

where d is the quantum dot diameter and

$$\frac{1}{m^*} = \frac{1}{m_e^*} + \frac{1}{m_h^*}, \quad (59)$$

with m_e^* and m_h^* being the electron and hole effective masses.

The experiments usually measure the optical gap of a quantum dot. Therefore, in addition to the difference in single-particle energies, one has to include the interaction between created electron and hole, in order to

calculate the optical gap. One simple approach to do this is to calculate the exciton energy by including the electron-hole interaction on top of the single-particle gap. This procedure ignores the electron-hole exchange interaction and possible correlation effects. However, in the strong confinement regime, which is present in most colloidal nanocrystals and embedded quantum dots, these effects are very small. Under this approximation, the exciton energy can be expressed as

$$E_{ex} = \epsilon_c - \epsilon_v - E_{cv}^C, \quad (60)$$

where ϵ_c and ϵ_v are the single-particle CBM and VBM energies and E_{cv}^C is the electron-hole Coulomb energy calculated as

$$E_{cv}^C = \int \int d\mathbf{r}_1 d\mathbf{r}_2 \frac{|\psi_c(\mathbf{r}_1)|^2 |\psi_v(\mathbf{r}_2)|^2}{\epsilon(\mathbf{r}_1 - \mathbf{r}_2) |\mathbf{r}_1 - \mathbf{r}_2|}, \quad (61)$$

where $\psi_c(\mathbf{r})$ and $\psi_v(\mathbf{r})$ are the electron and hole wave functions and $\epsilon(\mathbf{r}_1 - \mathbf{r}_2)$ is a distance dependent screening dielectric function, which can be modeled as described in [32].

The dependence of the calculated optical gap on CdSe nanocrystal size is presented in Fig. 5. A fit of the theoretical results to the

$$E_g = a \cdot d^{-\alpha}$$

dependence yields the values quite different from the simple d^{-2} law predicted from the effective mass approach. In the case of CdSe $\alpha = 1.18$. The α parameter is material dependent and its values for III-V and II-VI semiconductors typically fall in the range 1.1 – 1.7.

4.4 Excitons

In the previous section, we have presented the exciton calculations based on a simple, but useful approach. For the calculation of excitons the methods of Sec. 3 must be used in principle. The results of these methods are shown in Fig. 6 for H passivated Si quantum dots [137]. The DMC method and GW-BSE method produce almost the same band gap for the smallest quantum dots. The DMC result is about 1 eV above all the other results for somewhat larger quantum dots with the diameter up to 1.6 nm. It remains to be seen how accurate is this DMC result, for example when compared with well controlled experiments (perhaps for other material quantum dots like CdSe). The TDLDA method gives almost the same results as the LDA

Kohn Sham energy difference. This suggests that both the exchange and Coulomb interaction in the TDLDA results have a very small contribution. Besides TDLDA, TDDFT-B3LYP was used in Ref.[137] and Ref. [138]. The TDDFT-B3LYP band gap is below the DMC result, especially for relatively large quantum dots. However, in the work of Ref. [138], it was shown that for small molecules, the TDDFT-B3LYP result agrees with the MR-MP2 quantum chemistry calculations. The TB and EPM results in Fig. 6 can be considered as the lowest order results of the CI equation 43, where only the zero order screened Coulomb interactions between the VBM and CBM states are taken into account. These agree well with each other. However, they are between the TDLDA and TDDFT-B3LYP results.

To summarize these results, the DMC result is above all the other methods for $d = 1.5$ nm Si quantum dots. The LDA and TDLDA have the lowest band gap, followed by the TB and EPM limited CI results and the TDDFT-B3LYP results. For very small quantum dots, the DMC results agree well with the GW-BSE results.

4.5 Auger effects

Auger effects play a crucial role in carrier dynamics in nanostructures when both types of carriers (electrons and holes) are present. They become important in particular in quantum dots which have discrete electronic levels, which implies that the competing phonon-assisted relaxation processes are strongly reduced. Different types of Auger processes are schematically illustrated in Fig. 7.

According to Fermi's golden rule, the formula for the Auger rate is given as

$$W_i = \frac{2\pi}{\hbar} \sum_n |\langle i | \Delta H | f_n \rangle|^2 \delta(E_{f_n} - E_i), \quad (62)$$

where $|i\rangle$ and $|f_n\rangle$ are the initial and final Auger states, E_i and E_{f_n} their energies and ΔH is the Coulomb interaction. At a temperature $T \neq 0$ the Boltzmann average over the initial states has to be taken. It would seem at first sight that the discreteness of quantum dot energy levels and the requirement for energy conservation in the process, would not allow for efficient Auger processes. However, other excitations, such as phonons, can be involved as well, and help to satisfy the energy conservation. Their effect can then be phenomenologically modeled by Lorentzian broadening of the

delta function in Fermi's golden rule expression as

$$\delta(E_{f_n} - E_i) \rightarrow \frac{\Gamma}{2\pi} \frac{1}{(E_{f_n} - E_i)^2 + (\Gamma/2)^2}. \quad (63)$$

The most important step in the electron cooling process involves the transition of the electron from the p level (e_p) to the ground s electronic state (e_s). This process is mediated by a transition of the hole from h_s to h_n . The calculated Auger lifetime for this process is shown in Fig. 8. Its value is of the order of 0.1-0.5 ps, in agreement with experimental results [139]. This result suggests that Auger processes are sufficient to explain electron cooling in quantum dots, although other mechanisms are not necessarily ruled out.

The same process can take place in the presence of an electron and a hole that act only as spectators. It is very interesting that the electron lifetime increases by an order of magnitude in those cases, as demonstrated in Fig. 8.

4.6 Electron-phonon interaction

The theory and results presented so far covered only the stationary electronic structure of quantum dots when atoms are in their equilibrium positions. However, at finite temperatures the vibrations of atoms around their equilibrium positions (phonons) create additional potential that perturbs otherwise stationary electronic states and causes transitions among them.

Phonons in quantum dots can be treated at various levels of approximations. The approximation that is often used for large quantum dots is that the phonons are the same as in bulk material. The strongest coupling between electrons and phonons in polar crystals is polar coupling to longitudinal optical (LO) phonons, while deformation potential coupling to longitudinal acoustic (LA) phonons might also sometimes be important.

In order to calculate the transition rates among different electronic states due to the interaction with LO phonons, it is tempting to apply Fermi's Golden rule, which is a good approximation in quantum wells, for example [140]. However, its direct application to quantum dots leads to the result that transition rates are zero unless two levels are separated by one LO phonon energy exactly [141]. Such an approach treats the electron and phonon systems separately with their interaction being only a perturbation. It is currently known that electrons and phonons in quantum dots form coupled entities – polarons. Polarons in self-assembled quantum dots have so far been evidenced experimentally by optical means in the intraband

magneto-optical spectrum [142, 143], magnetophotoluminescence spectrum [144] and by Raman scattering [145] and it has been suggested theoretically that they could have transport signatures as well [146]. Polarons are usually evidenced by anticrossing of electron energy levels when these are gradually changed, such as for example by magnetic field. We illustrate this here by a numerical experiment where the energies of the pair of first excited states are shifted in opposite directions by the same amount ΔE , which is varied. The polaron states were calculated by direct diagonalization of the electron-phonon interaction Hamiltonian. The polaron energy levels that contain a contribution from at least one of the electronic states larger than 10% are shown by circles in Fig. 9. Anticrossing features in polaron spectrum are clearly visible.

There is therefore a widespread thought that carrier relaxation in quantum dots should be treated by considering the carriers as polarons. The polaron lifetime is then determined by anharmonic decay of an LO phonon into two low energy phonons [147, 142, 148, 149, 150]. It is thought that the physical process responsible for that decay process is either the decay to two LA phonons [151, 147] or to one acoustic and one optical phonon [150]. Within such assumptions, the polaron lifetime is in the case of a two level system given by [147]

$$W = \frac{\Gamma}{\hbar} - \frac{\sqrt{2(R - X)}}{\hbar}, \quad (64)$$

where $R = \sqrt{X^2 + Y^2}$, $X = g^2 + (\Delta^2 - \Gamma^2)/4$, $Y = \Gamma\Delta/2$, $\Delta = E_i - E_f - \hbar\omega_{\text{LO}}$, g is the electron-phonon coupling strength, Γ/\hbar the phonon decay rate, E_i and E_f the energies of the single particle states. Eq. (64) has been used in several occasions to fit the experimental results on intraband carrier dynamics in quantum dots [148, 152].

The approximation of bulk phonon modes certainly fails in small quantum dots. In that case, one should use the atomistic description of phonons. To calculate the phonon frequencies and displacements, one needs a force field which describes the vibrations of atoms around their equilibrium positions. VFF, for example, can be used for that purpose. To calculate the electron-phonon coupling, one needs to be able to calculate the change in single-particle Hamiltonian due to atomic displacements. Any of the single-particle methods described in Sec. 2 can in principle be used for that purpose. However, if some of the empirical methods is used, one should be sure that the fitted parameters are appropriate for this purpose, as well. Due to large number of atoms and consequently phonon modes, such calculations

could be quite expensive, nevertheless they are sometimes practiced. For example, Delerue, Allan and Lannoo [153] calculated the phonon modes in a Si nanocrystal using a valence force field model, and the coupling between the phonon modes and the transition electronic states explicitly using the Harrison's rule [56] for changes of TB parameters following the atomic displacements. Most recently, Chelikowsky et al. [154] calculated the phonons of Si quantum dots using direct DFT calculations.

5. CONCLUSIONS

We have given an overview of theoretical methods used for electronic structure calculations in quantum dots. We have emphasized the weaknesses and strengths of each of the methods. An interested reader can therefore choose the method of choice depending on the desired application, the degree of accuracy required and the available computational resources.

For the treatment of single-particle states, the simplest effective mass method is excellent for pedagogical purposes to illustrate the effect of quantum confinement. It is often even used in research when one wishes to qualitatively take into account the effect of quantum confinement and the details of the electronic structure are not essential. The multiband $\mathbf{k} \cdot \mathbf{p}$ method gives a more quantitative description, especially for large quantum dots. It is widely used in modeling of optical and transport processes in optoelectronic devices. Atomistic methods give a very detailed description of quantum dot electronic structure and are clearly the best choice in research for understanding the new physical effects.

For the treatment of excitations in quantum dots, Sec. 3 gives an overview of the methods that can be applied in principle. For application of these methods to quantum dots, linear scaling of the method is an essential requirement. CI approach satisfies this but it is based on classical model derivations and physical intuitions. QMC also appears to be promising. However, the method is relatively new, when the calculations of excited states and large systems are concerned. A deeper understanding of the accuracy, i.e. the quality of the variational form of the wave function or the nodal hypersurfaces, is required. When GW BSE approach is concerned, it is a challenge to make it scalable to larger systems.

ACKNOWLEDGEMENTS

This work was supported by U.S. Department of Energy BES/SC under

Contract number DE-AC02-05CH11231.

References

- [1] S. M. Reimann and M. Manninen, *Rev. Mod. Phys.* **74**, 1283 (2002).
- [2] W. G. van der Wiel, S. D. Franceschi, J. M. Elzerman, T. Fujisawa, S. Tarucha, and L. P. Kouwenhoven, *Rev. Mod. Phys.* **75**, 1 (2003).
- [3] J. Stangl, V. Holý, and G. Bauer, *Rev. Mod. Phys.* **76**, 725 (2004).
- [4] P. M. Petroff and S. P. DenBaars, **15**, 15 (1994).
- [5] D. Bimberg, M. Grundmann, and N. N. Ledentsov, *Quantum dot heterostructures* (John Wiley, Chichester, 1999).
- [6] A. P. Alivisatos, *Science* **271**, 933 (1996).
- [7] X. Michalet, F. F. Pinaud, L. A. Bentolila, J. M. Tsay, S. Doose, J. J. Li, G. Sundaresan, A. M. Wu, S. S. Gambhir, and S. Weiss, *Science* **307**, 538 (2005).
- [8] L. P. Kouwenhoven, D. G. Austing, and S. Tarucha, *Rep. Prog. Phys.* **64**, 701 (2001).
- [9] S. M. Cronenwett, T. H. Oosterkamp, and L. P. Kouwenhoven, *Science* **281**, 540 (1998).
- [10] D. Goldhaber-Gordon, H. Shtrikman, D. Mahalu, D. Abusch-Magder, U. Meirav, and M. A. Kastner, *Nature* **391**, 156 (1998).
- [11] A. Zrenner, E. Beham, S. Stuffer, F. Findeis, M. Bichler, and G. Abstreiter, *Nature* **418**, 612 (2002).
- [12] F. H. L. Koppens, C. Buizert, K. J. Tielrooij, I. T. Vink, K. C. Nowack, T. Meunier, L. P. Kouwenhoven, and L. M. K. Vandersypen, *Nature* **442**, 766 (2006).
- [13] J. R. Petta, A. C. Johnson, J. M. Taylor, E. A. Laird, A. Yacoby, M. D. Lukin, C. M. Marcus, M. P. Hanson, and A. C. Gossard, *Science* **309**, 2180 (2005).

- [14] R. Hanson, L. P. Kouwenhoven, J. R. Petta, S. Tarucha, and L. M. K. Vandersypen, *Rev. Mod. Phys.* **79**, 1217 (2007).
- [15] A. P. Alivisatos, W. W. Gu, and C. Larabell, *Ann. Rev. Biomed. Eng.* **7**, 55 (2005).
- [16] R. D. Schaller and V. I. Klimov, *Phys. Rev. Lett.* **92**, 186601 (2004).
- [17] N. Kirstaedter, N. N. Ledentsov, M. Grundmann, D. Bimberg, V. M. Ustinov, S. S. Ruvimov, M. V. Maximov, P. S. Kopev, Z. I. Alferov, U. Richter, P. Werner, U. Gosele, and J. Heydenreich, *Electron. Lett.* **30**, 1416 (1994).
- [18] P. Bhattacharya, S. Ghosh, and A. D. Stiff-Roberts, *Ann Rev. Mat. Res.* **34**, 1 (2004).
- [19] C. Santori, M. Pelton, G. S. Solomon, Y. Dale, and Y. Yamamoto, *Phys. Rev. Lett.* **86**, 1502 (2001).
- [20] P. Michler, A. Kiraz, C. Becher, W. V. Schoenfeld, P. M. Petroff, L. D. Zhang, E. Hu, and A. Imamoglu, *Science* **290**, 2282 (2000).
- [21] D. Pan, Y. P. Zeng, M. Y. Kong, J. Wu, Y. Q. Zhu, C. H. Zhang, J. M. Li, and C. Y. Wang, *Electron. Lett.* **32**, 1726 (1996).
- [22] D. Pan, E. Towe, and S. Kennerly, *Appl. Phys. Lett.* **73**, 1937 (1998).
- [23] S. Maimon, E. Finkman, G. Bahir, S. E. Schacham, J. M. Garcia, and P. M. Petroff, *Appl. Phys. Lett.* **73**, 2003 (1998).
- [24] L. E. Brus, *The Journal of Chemical Physics* **79**, 5566 (1983).
- [25] L. E. Brus, *The Journal of Chemical Physics* **80**, 4403 (1984).
- [26] P. Hohenberg and W. Kohn, *Phys. Rev.* **136**, B864 (1964).
- [27] W. Kohn and L. J. Sham, *Phys. Rev.* **140**, A1133 (1965).
- [28] L.-W. Wang, *Phys. Rev. Lett.* **88**, 256402 (2002).
- [29] L.-W. Wang, *Appl. Phys. Lett.* **78**, 1565 (2001).
- [30] J. Li and L.-W. Wang, *Phys. Rev. B* **67**, 033102 (2003).
- [31] J. Li and L.-W. Wang, *Phys. Rev. B* **67**, 205319 (2003).

- [32] J. Li and L.-W. Wang, Phys. Rev. B **72**, 125325 (2005).
- [33] L.-W. Wang, Phys. Rev. B **65**, 153410 (2002).
- [34] L.-W. Wang and A. Zunger, J. Chem. Phys. **100**, 2394 (1994).
- [35] N. Vukmirović and L.-W. Wang, J. Chem. Phys. **128**, 121102 (2008).
- [36] L.-S. Li and A. P. Alivisatos, Phys. Rev. Lett. **90**, 097402 (2003).
- [37] L.-W. Wang, Z. Zhao, and J. Meza, Phys. Rev. B **77**, 165113 (2008).
- [38] R. W. Godby, M. Schlüter, and L. J. Sham, Phys. Rev. B **37**, 10159 (1988).
- [39] M. S. Hybertsen and S. G. Louie, Phys. Rev. B **34**, 5390 (1986).
- [40] M. L. Cohen and T. K. Bergstresser, Phys. Rev. **141**, 789 (1966).
- [41] J. R. Chelikowsky and M. L. Cohen, Phys. Rev. B **14**, 556 (1976).
- [42] L.-W. Wang and A. Zunger, Phys. Rev. B **51**, 17398 (1995).
- [43] H. Fu and A. Zunger, Phys. Rev. B **55**, 1642 (1997).
- [44] M. P. Teter, M. C. Payne, and D. C. Allan, Phys. Rev. B **40**, 12255 (1989).
- [45] A. Canning, L. W. Wang, A. Williamson, and A. Zunger, J. Comp. Phys. **160**, 29 (2000).
- [46] L. W. Wang, J. Kim, and A. Zunger, Phys. Rev. B **59**, 5678 (1999).
- [47] L.-W. Wang, Phys. Rev. B **49**, 10154 (1994).
- [48] L.-W. Wang and A. Zunger, Phys. Rev. B **59**, 15806 (1999).
- [49] J. C. Slater and G. F. Koster, Phys. Rev. **94**, 1498 (1954).
- [50] T. Saito, J. N. Schulman, and Y. Arakawa, Phys. Rev. B **57**, 13016 (1998).
- [51] S. Lee, J. Kim, L. Jönsson, J. W. Wilkins, G. W. Bryant, and G. Klimeck, Phys. Rev. B **66**, 235307 (2002).

- [52] R. Santoprete, B. Koiller, R. B. Capaz, P. Kratzer, Q. K. K. Liu, and M. Scheffler, Phys. Rev. B **68**, 235311 (2003).
- [53] W. Sheng, S.-J. Cheng, and P. Hawrylak, Phys. Rev. B **71**, 035316 (2005).
- [54] P. Vogl, H. P. Hjalmarson, and J. D. Dow, J. Phys. Chem. Solids **44**, 365 (1983).
- [55] J.-M. Jancu, R. Scholz, F. Beltram, and F. Bassani, Phys. Rev. B **57**, 6493 (1998).
- [56] W. A. Harrison, *Electronic Structure and the Properties of Solids* (Freeman, San Francisco, 1980).
- [57] S. Y. Ren and J. D. Dow, Phys. Rev. B **45**, 6492 (1992).
- [58] N. A. Hill and K. B. Whaley, J. Chem. Phys. **100**, 2831 (1994).
- [59] M. G. Burt, J. Phys.: Condens. Matter **4**, 6651 (1992).
- [60] B. A. Foreman, Phys. Rev. Lett. **81**, 425 (1998).
- [61] J. M. Luttinger, Phys. Rev. **102**, 1030 (1956).
- [62] J. M. Luttinger and W. Kohn, Phys. Rev. **97**, 869 (1955).
- [63] C. R. Pidgeon and R. N. Brown, Phys. Rev. **146**, 575 (1966).
- [64] G. Bastard, *Wave Mechanics Applied to Semiconductor Heterostructures* (Les editions de physique, Les Ulis, 1992).
- [65] C. Pryor, Phys. Rev. B **57**, 7190 (1998).
- [66] O. Stier, M. Grundmann, and D. Bimberg, Phys. Rev. B **59**, 5688 (1999).
- [67] C. Pryor, Phys. Rev. Lett. **80**, 3579 (1998).
- [68] O. Stier, *Electronic and Optical Properties of Quantum Dots and Wires* (Wissenschaft & Technik Verlag, Berlin, 2000).
- [69] S. Tomić, A. G. Sunderland, and I. J. Bush, J. Mater. Chem. **16**, 1963 (2006).

- [70] B. A. Foreman, Phys. Rev. B **48**, 496 (1993).
- [71] B. A. Foreman, Phys. Rev. B **72**, 165345 (2005).
- [72] T. Nakaoka, T. Saito, J. Tatebayashi, and Y. Arakawa, Phys. Rev. B **70**, 235337 (2004).
- [73] H. Jiang and J. Singh, Phys. Rev. B **56**, 4696 (1997).
- [74] M. A. Cusack, P. R. Briddon, and M. Jaros, Phys. Rev. B **54**, R2300 (1996).
- [75] S.-S. Li, J.-B. Xia, Z. L. Yuan, Z. Y. Xu, W. Ge, X. R. Wang, Y. Wang, J. Wang, and L. L. Chang, Phys. Rev. B **54**, 11575 (1996).
- [76] A. D. Andreev and E. P. O'Reilly, Phys. Rev. B **62**, 15851 (2000).
- [77] N. Vukmirović, D. Indjin, V. D. Jovanović, Z. Ikonić, and P. Harrison, Phys. Rev. B **72**, 075356 (2005).
- [78] S. Tomić, Phys. Rev. B **73**, 125348 (2006).
- [79] V. Mlinar, M. Tadić, and F. M. Peeters, Phys. Rev. B **73**, 235336 (2006).
- [80] M. Tadić, F. M. Peeters, and K. L. Janssens, Phys. Rev. B **65**, 165333 (2002).
- [81] N. Vukmirović, Ž. Gačević, Z. Ikonić, D. Indjin, P. Harrison, and V. Milanović, Semicond. Sci. Technol. **21**, 1098 (2006).
- [82] M. Roy and P. A. Maksym, Phys. Rev. B **68**, 235308 (2003).
- [83] H. Fu, L.-W. Wang, and A. Zunger, Phys. Rev. B **57**, 9971 (1998).
- [84] L.-W. Wang and A. Zunger, The Journal of Physical Chemistry B **102**, 6449 (1998).
- [85] L.-W. Wang, Phys. Rev. B **61**, 7241 (2000).
- [86] N. Vukmirović and S. Tomić, J. Appl. Phys. **103**, 103718 (2008).
- [87] N. Vukmirović, Z. Ikonić, D. Indjin, and P. Harrison, J. Phys.: Condens. Matter **18**, 6249 (2006).

- [88] P. N. Keating, Phys. Rev. **145**, 637 (1966).
- [89] R. M. Martin, Phys. Rev. B **1**, 4005 (1970).
- [90] C. Pryor, J. Kim, L. W. Wang, A. J. Williamson, and A. Zunger, J. Appl. Phys. **83**, 2548 (1998).
- [91] A. J. Williamson, L. W. Wang, and A. Zunger, Phys. Rev. B **62**, 12963 (2000).
- [92] T. B. Boykin, G. Klimeck, R. C. Bowen, and F. Oyafuso, Phys. Rev. B **66**, 125207 (2002).
- [93] Y. M. Niquet, D. Rideau, C. Tavernier, H. Jaouen, and X. Blase, Phys. Rev. B **79**, 245201 (2009).
- [94] J.-M. Jancu and P. Voisin, Phys. Rev. B **76**, 115202 (2007).
- [95] M. Tadić, F. M. Peeters, K. L. Janssens, M. Korkusiński, and P. Hawrylak, J. Appl. Phys. **92**, 5819 (2002).
- [96] A. D. Andreev, J. R. Downes, D. A. Faux, and E. P. O'Reilly, J. Appl. Phys. **86**, 297 (1999).
- [97] J. H. Davies, J. Appl. Phys. **84**, 1358 (1998).
- [98] G. Bester, X. Wu, D. Vanderbilt, and A. Zunger, Physical Review Letters **96**, 187602 (2006).
- [99] E. Gross, F. Dobson, and M. Petersilka, *Density Functional Theory* (Springer, New York, 1996).
- [100] K. Burke, M. Petersilka, and E. Gross, *A hybrid functional for the exchange-correlation kernel in time-dependent density functional theory*, Recent Advances in Density Functional Methods Vol. 3 (World Scientific, Singapore, 2002), pp. 67–79.
- [101] K. Yabana and G. F. Bertsch, Phys. Rev. B **54**, 4484 (1996).
- [102] L. X. Benedict, A. Puzder, A. J. Williamson, J. C. Grossman, G. Galli, J. E. Klepeis, J.-Y. Raty, and O. Pankratov, Phys. Rev. B **68**, 085310 (2003).
- [103] I. V. Tokatly and O. Pankratov, Phys. Rev. Lett. **86**, 2078 (2001).

- [104] I. V. Tokatly, R. Stubner, and O. Pankratov, Phys. Rev. B **65**, 113107 (2002).
- [105] P. J. Stephens, F. H. Devlin, C. F. Chabalowski, and M. J. Frisch, J. Phys. Chem. **98**, 11623 (1994).
- [106] J. Muscat, A. Wander, and N. M. Harrison, Chemical Physics Letters **342**, 397 (2001).
- [107] L. X. Benedict, Phys. Rev. B **66**, 193105 (2002).
- [108] A. Franceschetti, L. W. Wang, H. Fu, and A. Zunger, Phys. Rev. B **58**, R13367 (1998).
- [109] L. C. Andreani, F. Bassani, and A. Quattropani, Nuovo Cimento Della Societa Italiana di Fisica D **10**, 1473 (1988).
- [110] K. Cho, Solid State Communications **33**, 911 (1980).
- [111] G. Bester, S. Nair, and A. Zunger, Phys. Rev. B **67**, 161306 (2003).
- [112] L.-W. Wang, M. Califano, A. Zunger, and A. Franceschetti, Phys. Rev. Lett. **91**, 056404 (2003).
- [113] G. Onida, L. Reining, and A. Rubio, Rev. Mod. Phys. **74**, 601 (2002).
- [114] L. Hedin, Phys. Rev. **139**, A796 (1965).
- [115] P. Sánchez-Friera and R. W. Godby, Phys. Rev. Lett. **85**, 5611 (2000).
- [116] P. García-González and R. W. Godby, Phys. Rev. Lett. **88**, 056406 (2002).
- [117] F. Aryasetiawan, T. Miyake, and K. Terakura, Phys. Rev. Lett. **88**, 166401 (2002).
- [118] C. Verdozzi, R. W. Godby, and S. Holloway, Phys. Rev. Lett. **74**, 2327 (1995).
- [119] A. Schindlmayr, T. J. Pollehn, and R. W. Godby, Phys. Rev. B **58**, 12684 (1998).
- [120] G. Strinati, Phys. Rev. B **29**, 5718 (1984).
- [121] M. Rohlfing and S. G. Louie, Phys. Rev. B **62**, 4927 (2000).

- [122] A. Franceschetti and A. Zunger, Phys. Rev. B **62**, 2614 (2000).
- [123] C. Delerue, M. Lannoo, and G. Allan, Phys. Rev. Lett. **84**, 2457 (2000).
- [124] M. Rohlfing and S. G. Louie, Phys. Rev. Lett. **80**, 3320 (1998).
- [125] S. Ögüt, J. R. Chelikowsky, and S. G. Louie, Phys. Rev. Lett. **79**, 1770 (1997).
- [126] W. M. C. Foulkes, L. Mitas, R. J. Needs, and G. Rajagopal, Rev. Mod. Phys. **73**, 33 (2001).
- [127] P. J. Reynolds, D. M. Ceperley, B. J. Alder, and W. A. Lester, The Journal of Chemical Physics **77**, 5593 (1982).
- [128] C. J. Umrigar, K. G. Wilson, and J. W. Wilkins, Phys. Rev. Lett. **60**, 1719 (1988).
- [129] D. Ceperley, G. V. Chester, and M. H. Kalos, Phys. Rev. B **16**, 3081 (1977).
- [130] B. Hammond, J. W.A. Lester, and P. Reynolds, *Monte Carlo Methods in Ab Initio Quantum Chemistry* (World Scientific, Singapore, 1994).
- [131] S. Fahy, X. W. Wang, and S. G. Louie, Phys. Rev. B **42**, 3503 (1990).
- [132] A. J. Williamson, R. Q. Hood, R. J. Needs, and G. Rajagopal, Phys. Rev. B **57**, 12140 (1998).
- [133] A. J. Williamson, R. Q. Hood, and J. C. Grossman, Phys. Rev. Lett. **87**, 246406 (2001).
- [134] A. Puzder, A. J. Williamson, J. C. Grossman, and G. Galli, Phys. Rev. Lett. **88**, 097401 (2002).
- [135] J. Even, F. Doré, C. Cornet, and L. Pedesseau, Phys. Rev. B **77**, 085305 (2008).
- [136] Z. Chen, O. Baklenov, E. T. Kim, I. Mukhametzhanov, J. Tie, A. Madhukar, Z. Ye, and J. C. Campbell, J. Appl. Phys. **89**, 4558 (2001).
- [137] A. J. Williamson, J. C. Grossman, R. Q. Hood, A. Puzder, and G. Galli, Phys. Rev. Lett. **89**, 196803 (2002).

- [138] C. S. Garoufalidis, A. D. Zdetsis, and S. Grimme, Phys. Rev. Lett. **87**, 276402 (2001).
- [139] V. I. Klimov, The Journal of Physical Chemistry B **104**, 6112 (2000).
- [140] P. Harrison, *Quantum Wells, Wires and Dots*, 2nd edition (John Wiley and Sons Ltd., Chichester, England, 2005).
- [141] U. Bockelman and G. Bastard, Phys. Rev. B **42**, 8947 (1990).
- [142] S. Hameau, Y. Guldner, O. Verzelen, R. Ferreira, G. Bastard, J. Zeman, A. Lemaître, and J. M. Gérard, Phys. Rev. Lett. **83**, 4152 (1999).
- [143] P. A. Knipp, T. L. Reinecke, A. Lorke, M. Fricke, and P. M. Petroff, Phys. Rev. B **56**, 1516 (1997).
- [144] V. Preisler, T. Grange, R. Ferreira, L. A. de Vaultier, Y. Guldner, F. J. Teran, M. Potemski, and A. Lemaitre, Phys. Rev. B **73**, 075320 (2006).
- [145] B. Aslan, H. C. Liu, M. Korkusinski, P. Hawrylak, and D. J. Lockwood, Phys. Rev. B **73**, 233311 (2006).
- [146] N. Vukmirović, Z. Ikonić, D. Indjin, and P. Harrison, Phys. Rev. B **76**, 245313 (2007).
- [147] X.-Q. Li, H. Nakayama, and Y. Arakawa, Phys. Rev. B **59**, 5069 (1999).
- [148] S. Sauvage, P. Boucaud, R. P. S. M. Lobo, F. Bras, G. Fishman, R. Prazeres, F. Glotin, J. M. Ortega, and J.-M. Gérard, Phys. Rev. Lett. **88**, 177402 (2002).
- [149] J. Urayama, T. B. Norris, J. Singh, and P. Bhattacharya, Phys. Rev. Lett. **86**, 4930 (2001).
- [150] O. Verzelen, R. Ferreira, and G. Bastard, Phys. Rev. B **62**, R4809 (2000).
- [151] A. R. Bhat, K. W. Kim, and M. A. Strosio, J. Appl. Phys. **76**, 3905 (1994).
- [152] E. A. Zibik, L. R. Wilson, R. P. Green, G. Bastard, R. Ferreira, P. J. Phillips, D. A. Carder, J.-P. R. Wells, J. W. Cockburn, M. S. Skolnick, M. J. Steer, and M. Hopkinson, Phys. Rev. B **70**, 161305 (2004).

- [153] C. Delerue, G. Allan, and M. Lannoo, Phys. Rev. B **64**, 193402 (2001).
- [154] J. R. Chelikowsky, A. T. Zayak, T.-L. Chan, M. L. Tiago, Y. Zhou, and Y. Saad, Journal of Physics: Condensed Matter **21**, 064207 (2009).
- [155] C. B. Murray, D. J. Norris, and M. G. Bawendi, Journal of the American Chemical Society **115**, 8706 (1993).

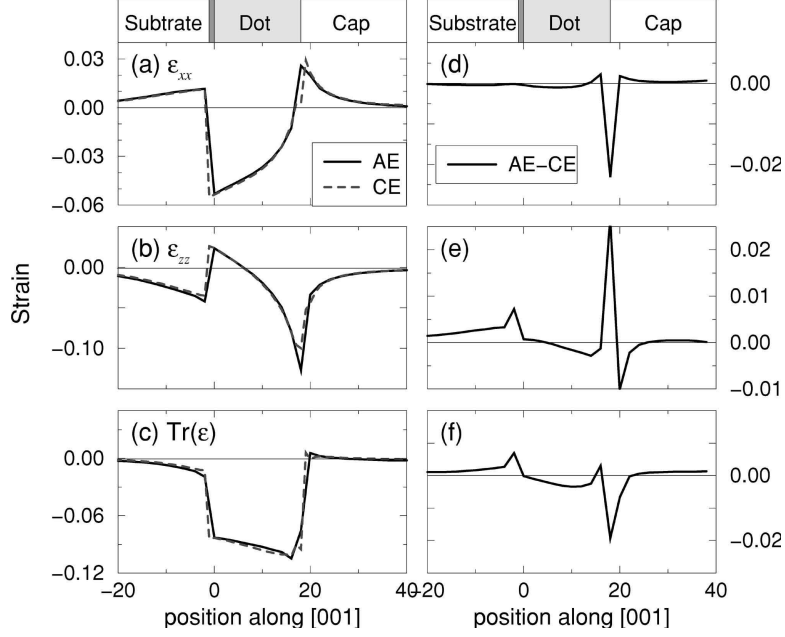


Figure 1: Strain profiles of InAs/GaAs square-based pyramidal quantum dots and the differences along the z -direction through the pyramidal tip. The differences between the continuum elasticity (CE) and atomistic elasticity (AE) are given on the right-hand side. The discrepancy is the largest around the interfaces, while the strains in the barrier (GaAs substrate and capping layer) agree well within 0.5%. A significant difference is also found inside the quantum dot where the InAs experience large compressive strains at about 7% due to the lattice mismatch. Reprinted figure with permission from Ref. [90] C. Pryor, J. Kim, L. W. Wang and A. Zunger, J. Appl. Phys. **83**, 2548 (1998). Copyright (1998) by the American Institute of Physics.

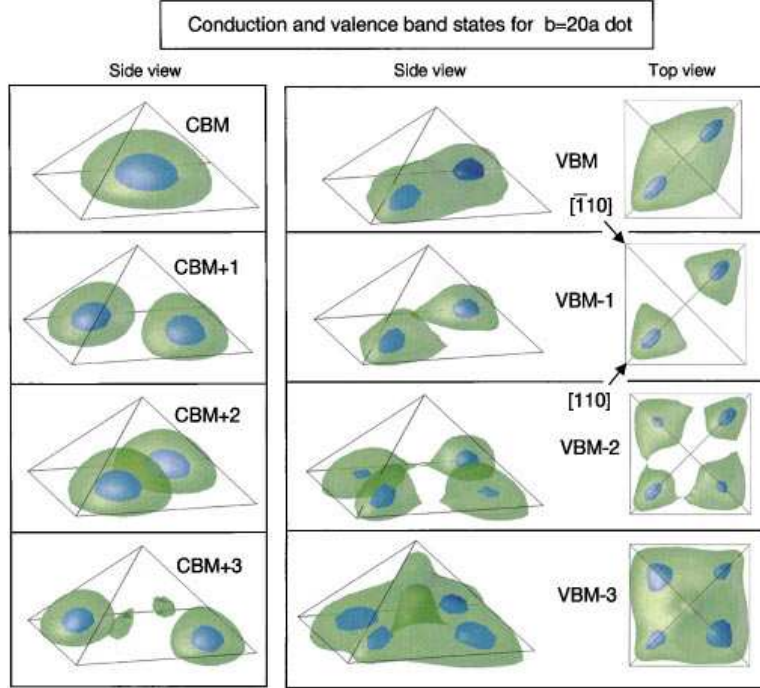


Figure 2: Isosurface plots of the charge densities of the conduction and valence band states for the square based InAs/GaAs pyramids with the base $b = 20a$, where a is the lattice constant of bulk zincblende GaAs. The charge density equals the wave-function square, including the spin-up and -down components. The level values of the green and blue isosurfaces equal 0.25 and 0.75 of the maximum charge density, respectively. Reprinted figure with permission from [46], L. W. Wang, J. Kim and A. Zunger, Phys. Rev. B **59**, 5678 (1999). Copyright (1999) by the American Physical Society.

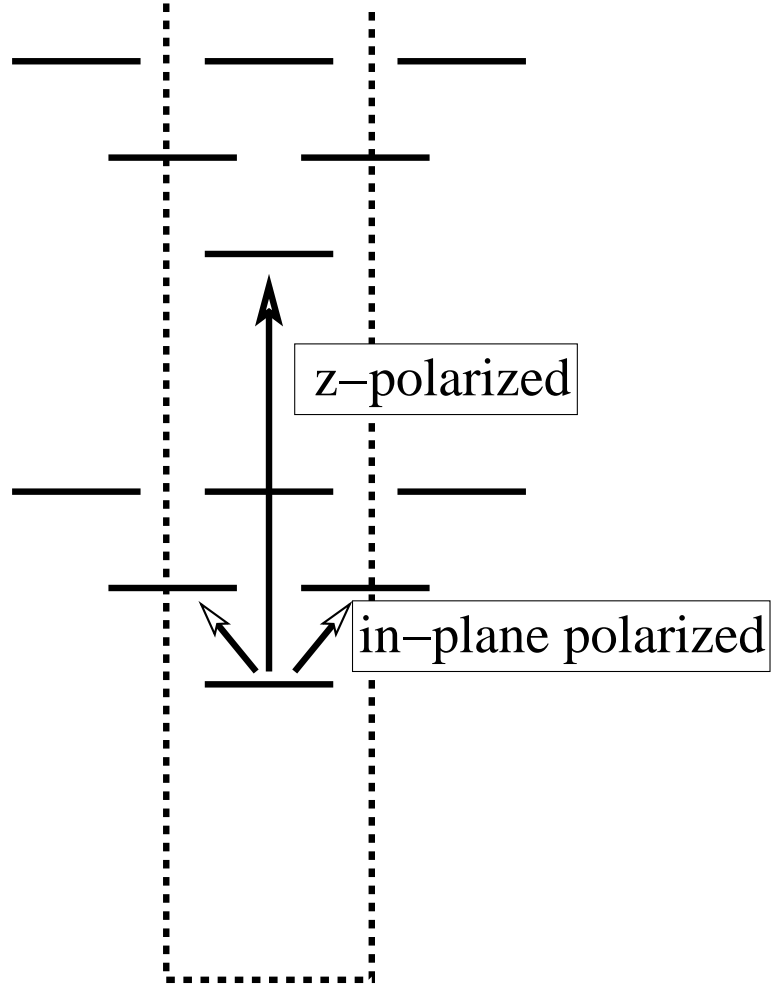


Figure 3: Scheme of energy levels and allowed optical transitions in a parabolic quantum dot model with infinite potential barriers. Only the levels with $n_x + n_y \leq 2$ and $n_z \leq 2$ are shown.

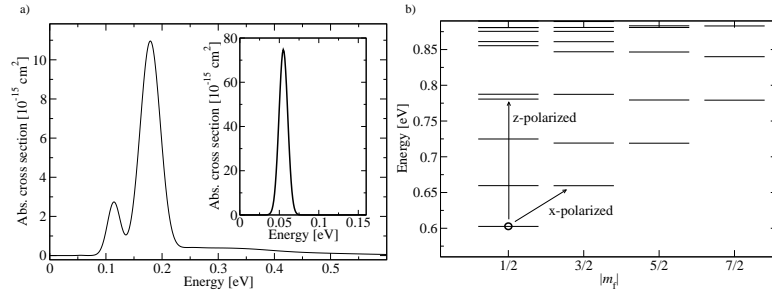


Figure 4: a) The intraband optical absorption spectrum for a quantum dot of conical shape with the diameter $D = 25$ nm and height $h = 7$ nm for the case of z -polarized radiation. The corresponding spectrum for in-plane polarized radiation is shown in the inset. b) The scheme of energy levels and the most relevant transitions. The quantum number of total quasi-angular momentum m_f which is a good quantum number in the case of axially symmetric quantum dots within the axial approximation of 8-band $\mathbf{k} \cdot \mathbf{p}$ model is also indicated.

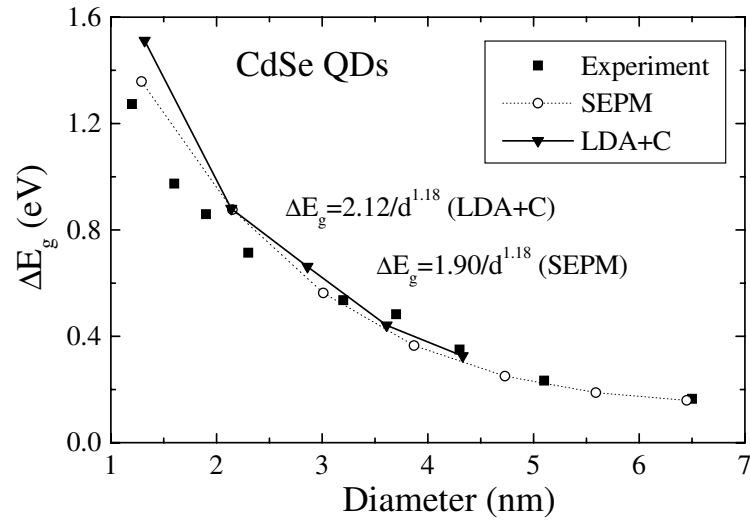


Figure 5: Comparison of the exciton energy shift from its bulk value of CdSe QDs between experiment, charge patching method (with band gap corrected pseudopotentials) (LDA+C), and SEPM calculations. Coulomb energies are considered in this calculation. Experimental data is from Ref. [155]. Reprinted figure with permission from Ref. [32], J. Li and L. W. Wang, Phys. Rev. B **72**, 125325 (2005). Copyright (2005) by the American Physical Society.

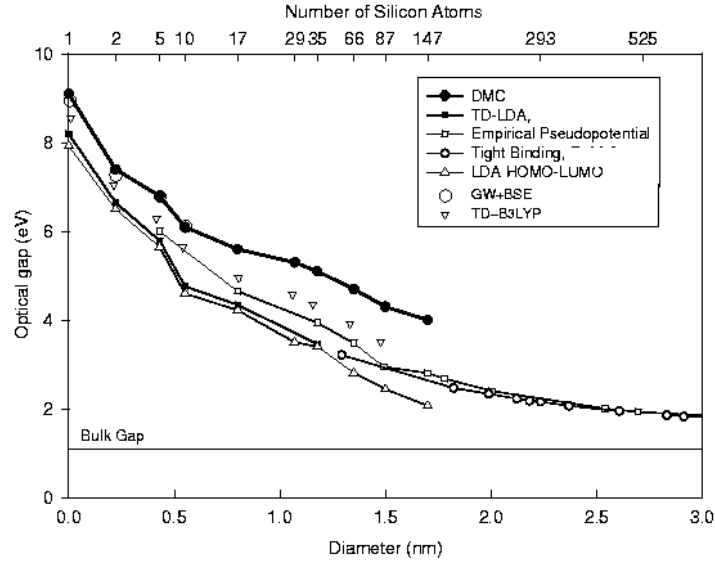


Figure 6: Size dependence of optical gaps of silicon nanoclusters, calculated using diffusion Monte Carlo (DMC), GW-BSE, LDA, and time dependent LDA (TDLDA), time dependent DFT with B3LYP functional (TDDFT-B3LYP), semiempirical tight-binding and semiempirical pseudopotential methods. Note the DMC and GW-BSE results are almost the same for the few small clusters. Reprinted figure with permission from [137], A.J. Williamson, J.C. Grossman, R.Q. Hood, A. Puzder, G. Galli, Phys. Rev. Lett. **89**, 196803 (2002). Copyright (2002) by the American Physical Society.

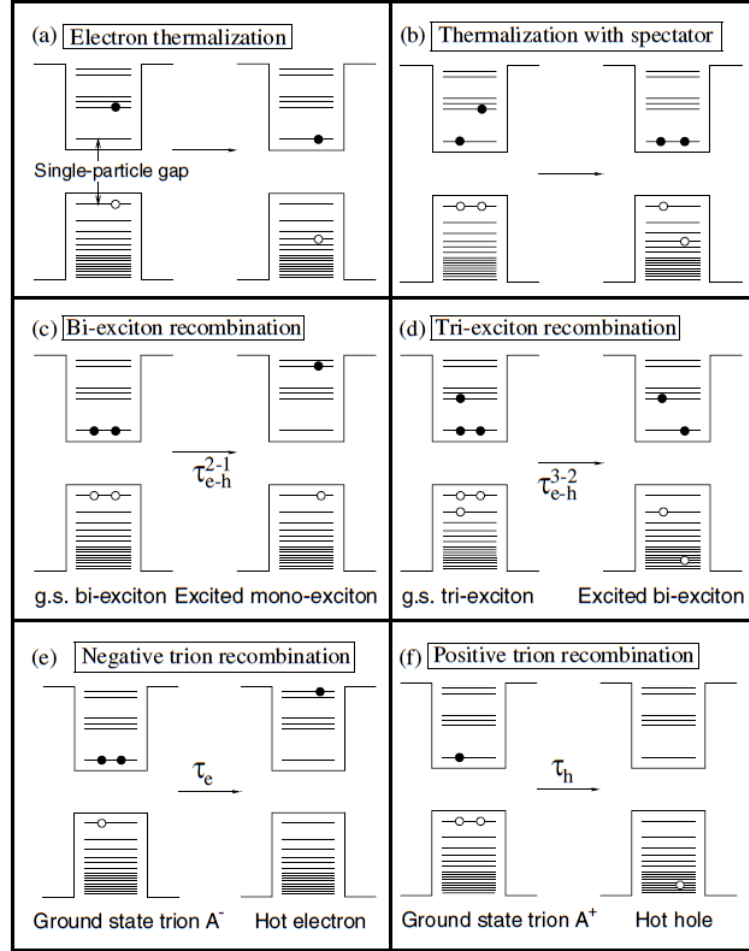


Figure 7: Illustration of different possible Auger processes. Reprinted figure with permission from [112], L. W. Wang, M. Califano, A. Zunger and A. Franceschetti, Phys. Rev. Lett. **91**, 056404 (2003). Copyright (2003) by the American Physical Society.

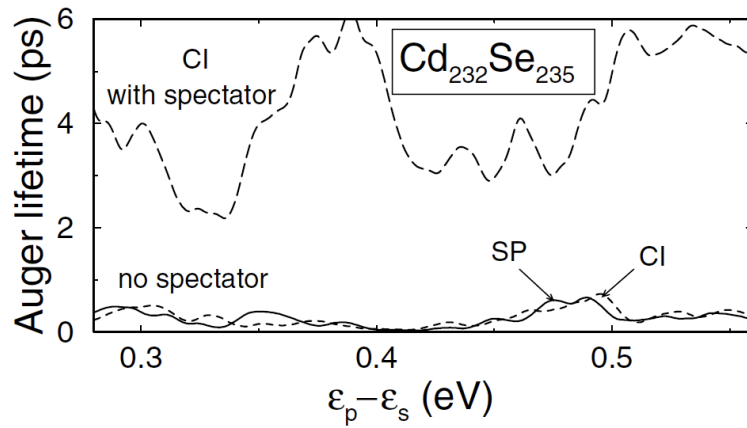


Figure 8: Electron cooling. Auger lifetimes at $T = 300$ K calculated with EPM within the single-particle (SP) approximation (solid line), and with CI, both in the absence (dashed line) and in the presence (long-dashed line) of a spectator ground state exciton. The initial states include all three electron p states and both hole s states, and the final states e_s and 30 hole states h_n with energy centered around $E_{n0} = \epsilon_{h_s} - \epsilon_{e_p} + \epsilon_{e_s}$. Reprinted figure with permission from [112], L. W. Wang, M. Califano, A. Zunger and A. Franceschetti, Phys. Rev. Lett. **91**, 056404 (2003). Copyright (2003) by the American Physical Society.

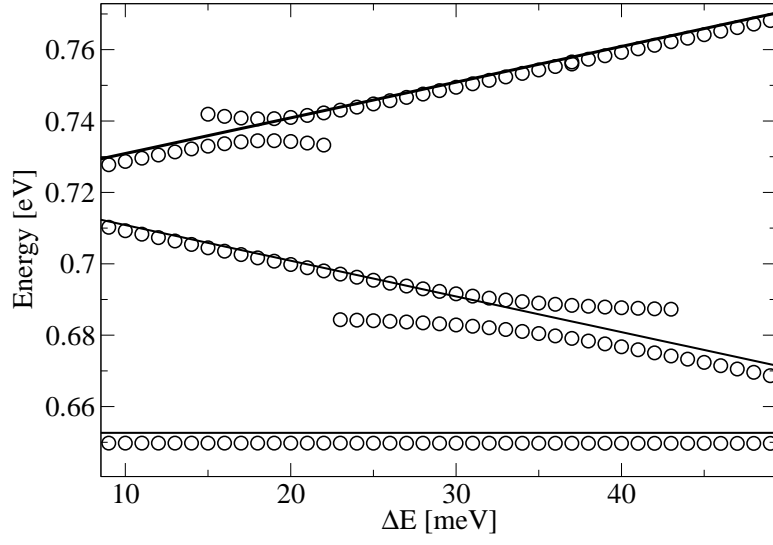


Figure 9: Dependence of the polaron energy levels obtained by direct diagonalization (circles) on the artificial shift ΔE . The corresponding single-particle levels calculated using the 8-band $\mathbf{k} \cdot \mathbf{p}$ model are shown by full lines. Lens-shaped quantum dot with the diameter of 20 nm and the height of 5 nm is considered.